Inorganic Chemistry

pubs.acs.org/IC

Article

Potent Half-Sandwich 16-/18-Electron Iridium(III) and Ruthenium(II) Anticancer Complexes with Readily Available Amine−Imine Ligands

Lihua Guo,* Pengwei Li, Jiaxing Li, Yuwen Gong, Xiaoyuan Li, Tingjun Wen, Xinxin Wu, Xinyi Yang, and Zhe Liu*

Cite This: *Inorg. Chem.* 2023, 62, 21379−21395

Read Online

ACCESS | Metrics & More | Article Recommendations | Supporting Information

ABSTRACT: The synthesis and biological evaluation of stable 16-electron half-sandwich complexes have remained scarce. We herein present the different coordination modes (16-electron or 18-electron) between half-sandwich iridium(III) complexes and ruthenium(II) complexes derived from the same amine−imine ligands chelating hybrid sp^3-N/sp^2-N donors. The 16-electron iridium(III) and 18-electron ruthenium(II) complexes with different counteranions were obtained and identified by various techniques. The promising cytotoxicity of these complexes against A549 lung cancer cells, cisplatin-resistant A549/DPP cells, cervical carcinoma HeLa cells, and human hepatocellular liver carcinoma HepG2 cells was observed with IC_{50} values ranging from 5.4 to 16.3 μM. Moreover, these complexes showed a certain selectivity (selectivity index: 2.1−3.7) toward A549 cells and BEAS-2B normal cells. The variation of metal center, counteranion, 16/18-electron coordination mode, and ligand substituents showed little influence on the cytotoxicity and selectivity of these complexes. The mechanism of action study showed that these complexes could target mitochondria, induce the depolarization of the mitochondrial membrane, and promote the generation of intracellular reactive oxygen species (ROS). Further, the induction of cell apoptosis and the perturbation of the cell cycle in the G_0/G_1 phase were also observed for these complexes. Overall, it seems that the redox mechanism dominated the anticancer efficacy of these complexes.

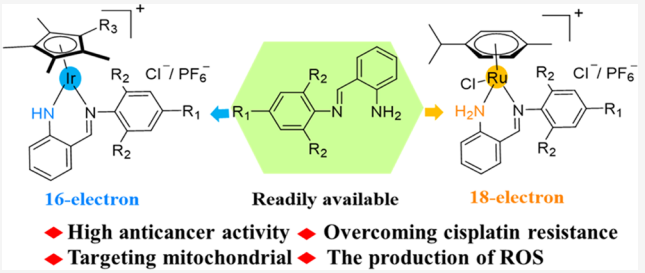

1. INTRODUCTION

Chemotherapy has been the primary approach to cancer treatment, despite significant advancements over the past 50 years. Platinum-based drugs, which mainly comprised cisplatin, carboplatin, and oxaliplatin, have been well-studied in treating various tumors.[1,2] However, these anticancer drugs lack selectivity, have many serious side effects, and can lead to drug resistance.[3−6] As a result, many research efforts have focused on developing alternative anticancer complexes with high selectivity and novel mechanisms of action (MoAs) to reduce side effects and overcome drug resistance.[7−12] Various complexes of platinum group metals, including iridium, rhodium, ruthenium, and osmium, have been developed for this purpose. In particular, azole-based ruthenium complexes, NAMI-A and KP1019, have entered clinical trials.[13,14]

In the last decade, platinum group-based half-sandwich anticancer complexes of the formula $[(\eta^5\text{-Cp}^x)/(\eta^6\text{-arene})\text{M-(XY)Z}]^{0/+}$ (XY = bidentate chelating ligand; Z = monodentate labile ligand, mostly chosen as Cl^-; Cp^x = substituted cyclopentadienyl; M = iridium, rhodium, ruthenium, and osmium) have provided a versatile and simple platform for developing new organometallic anticancer drugs due to their structural diversity and unique MoAs.[15−20] The majority of these studies have been directed toward the synthesis and investigation of 18-electron cationic and neutral anticancer complexes using different bidentate XY chelating ligands. Notably, XY has mostly been chosen as an N,N donor among these complexes. One of the important N,N-chelating arene−ruthenium(II) anticancer complexes was RM175 containing an ethylenediamine (en) ligand (Scheme 1, **I**), which has achieved success in both in vitro and in vivo cytotoxic assessments.[21] Moreover, RM175 did not reveal any cross-resistance against cisplatin-resistant A2780cis cells, suggesting a distinctive mode of anticancer action.[22,23] Sadler and co-workers have shown that iridium(III) complexes bearing N,N-chelating bipyridine (bpy) were approximately twice as potent than cisplatin against A2780 cancer cell line (Scheme 1, **II**). The enhanced anticancer efficiency of these complexes was due to their increased hydrophobicity and DNA-binding activities.[24] The Os(II) complex FY-26 with the asymmetric N,N-chelating donor has a novel mechanism of action centered on inducing dysfunctional mitochondria and increasing reactive oxygen species (ROS) levels, thereby allowing it

Received: October 4, 2023
Revised: November 27, 2023
Accepted: November 28, 2023
Published: December 14, 2023

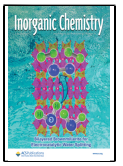

Scheme 1. Reported Organometallic N,N-chelating Half-Sandwich Platinum Group Metal Complexes and Our Current Work

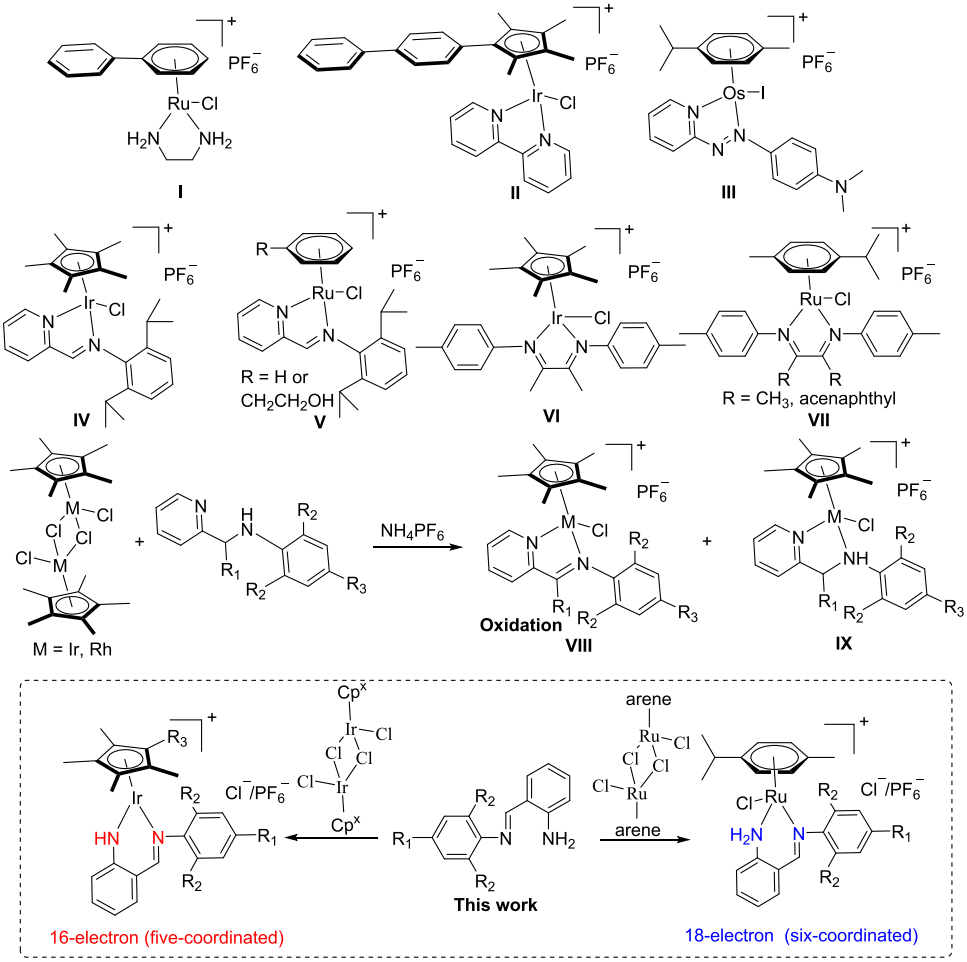

possible to combat cancer cell drug resistance and exert selective activity toward cancer cells and normal cells (Scheme 1, **III**).[25−27] Our group has also been working to develop a series of platinum group-based half-sandwich complexes with N,N-chelating ligand systems. For example, the pyridyl-imine half-sandwich iridium(III) and ruthenium(II) complexes were able to convert nicotinamide adenine dinucleotide (NADH) to NAD^+, increase ROS levels, disrupt mitochondrial membranes (causing mitochondrial dysfunction), and show promising cytotoxicity toward A549 and HeLa cells (Scheme 1, **IV** and **V**).[28−30] Due to the constant oxidative stress caused by high levels of ROS generation, cancer cells are highly sensitive to changes in the cell's redox state.[31] Some selected pyridyl-imine ruthenium(II) complexes displayed anticancer selectivity toward A549 cells over BEAS-2B cells (Scheme 1, **V**).[29,30] In addition, a set of iridium(III) and ruthenium(II) complexes with α-diimine N,N-chelating ligands were also prepared. These complexes can induce cell apoptosis through ROS-mediated signaling and display no cross-resistance with cisplatin (Scheme 1, **VI** and **VII**).[32−34]

Mitochondria are closely associated with a variety of cellular processes, such as energy generation, apoptotic induction, and redox signaling.[32,35,36] Cancer cells show varying degrees of mitochondrial dysfunction, such as altered energy metabolism, higher mitochondrial membrane potential (MMP), and increased oxidative stress. These characteristics offer chances to target cancer cell mitochondria for an optimal therapeutic outcome.[37] Mitochondrial-targeting drugs usually exhibit two main characteristics: high positive charge and strong hydrophobicity.[38] Since cancer cells have a higher mitochondria membrane potential compared to normal cells,[39] the hydrophobic cations tend to accumulate more in the mitochondria of cancer cells. Furthermore, drugs with strong hydrophobic properties can increase their affinity with mitochondrial membranes, leading to disruption of normal metabolic homeostasis and dysregulation of intracellular ROS levels.[40−42]

It should be noted that the coordination fashion of the above-mentioned N,N-chelating complexes was sp^3-N/sp^3-N amine−metal (H_2N → metal, Scheme 1, **I**) or sp^2-N/sp^2-N imine−metal (C═N → metal, Scheme 1, **II**−**VII**). We were interested in extending our research to hybrid sp^3-N/sp^2-N chelating complexes. However, our preliminary attempt to obtain these complexes using sp^3-N/sp^2-N pyridyl-amine ligands generated a mixture of pyridyl-imine (sp^2-N/sp^2-N) and pyridyl-amine (sp^3-N/sp^2-N) complexes due to their easily oxidizable nature, which made it difficult to investigate the anticancer efficiency of these sp^3-N/sp^2-N-chelating complexes (Scheme 1, **VIII** and **IX**).[43] Herein, based on the [NH_2, N] Schiff base ligands, we prepared a series of amine−imine (sp^3-N/sp^2-N) half-sandwich iridium(III) and ruthenium(II) complexes (Scheme 2). It was surprising that this simple and readily accessible Schiff base, which showed the hybrid sp^3-N/sp^2-N donor, has not yet been used in synthesizing platinum group metal-based half-sandwich complexes. The different

https://doi.org/10.1021/acs.inorgchem.3c03471
Inorg. Chem. 2023, 62, 21379−21395

Scheme 2. Synthesis of Amine−Imine Ligands (a) and the Corresponding Half-Sandwich Iridium(III) and Ruthenium(II) Complexes with Cl^- (b) and PF_6^- (c) as Counteranions

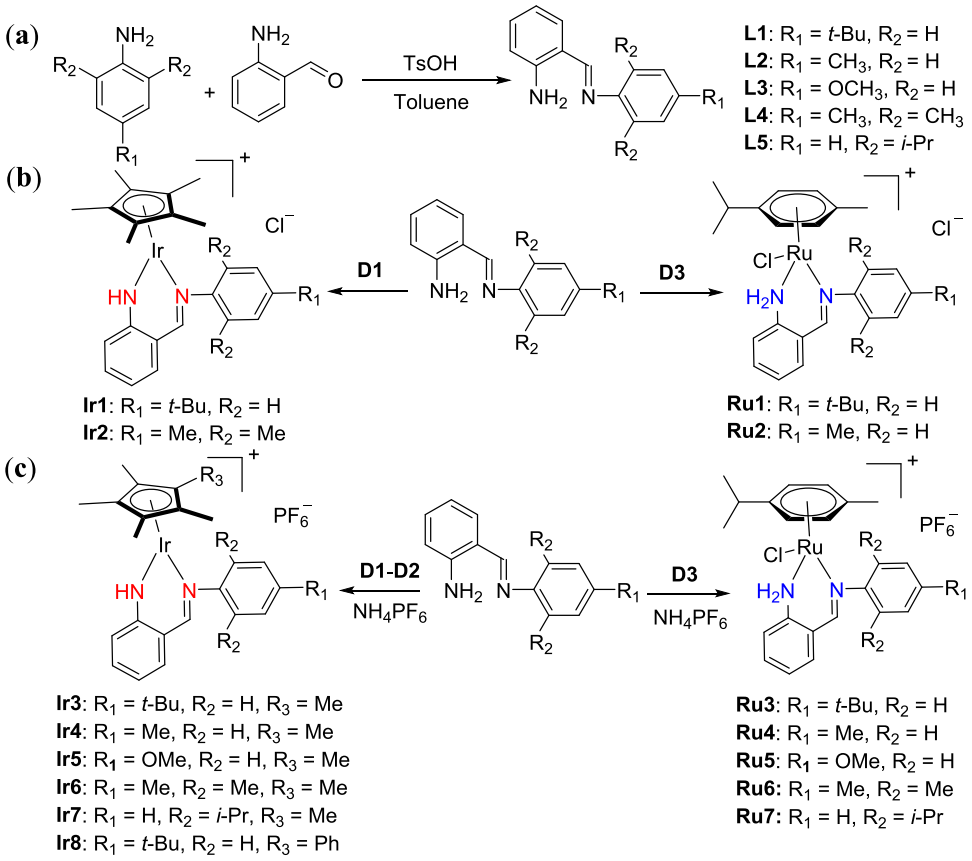

coordination modes between iridium(III) (16-electron, five-coordinated, without monodentate labile Cl^-) and ruthenium-(II) (18-electron, six-coordinated) complexes were observed. Notably, the synthesis of stable 16-electron platinum group metal-based half-sandwich complexes and their biological evaluation have been rarely reported.[44] All of the complexes in this system were highly active toward several cancer cell lines, showed the ability to circumvent platinum resistance, and exhibited certain selectivity toward cancer cells over normal cells. In particular, their possible MoAs in vitro, including mitochondria-targeting, ROS production, and cell apoptosis, were determined.

2. RESULTS AND DISCUSSION

2.1. Synthesis and Characterizations. The amine−imine Schiff base ligands **L1−L5** can be easily prepared from a simple single-step *p*-toluenesulfonic acid (TsOH)-catalyzed reaction of 2-aminobenzaldehyde with anilines in 67−74% isolated yields (Scheme 2a). Ligands **L2−L5** were previously known.[45,46] The identity of ligand **L1** was also verified by ^{1}H NMR (Figure S1), $^{13}C\{^1H\}$ NMR (Figure S2), and mass spectrometry (Figure S35). This type of amine−imine ligand provides an easy-to-handle, cheap, and versatile platform for the development of platinum group metal-based half-sandwich complexes chelating hybrid sp^3-N/sp^2-N donors.

The chloro-bridged bimetallic iridium(III) precursors **D1** ($[(\eta^5\text{-Cp}^*)IrCl_2]_2$), **D2** ($[(\eta^5\text{-Cp}^{ph})IrCl_2]_2$), and ruthenium-(II) precursor **D3** ($[(\eta^6\text{-}p\text{-cymene})RuCl_2]_2$) were prepared according to the literature.[44,47] Reactions of **D1** and **D3** with the corresponding amine−imine ligands in CH_3OH/CH_2Cl_2 (v/v, ca. 1/1) at room temperature yielded 16-electron [NH, N]-coordinated iridium(III) complexes **Ir1−Ir2** and 18-electron [NH_2, N]-coordinated ruthenium(II) complexes **Ru1−Ru2** as Cl^- salts (Scheme 2b), Cl^- as the counteranion with the formula of $[(\eta^5\text{-Cp}^x)Ir(NH, N)Cl]Cl$ and ($[(\eta^6\text{-}p\text{-cymene})Ru(NH_2, N)Cl]Cl$). Likewise, treatment of **D1−D3** with ligands **L1−L5** and an excess of ammonium salt NH_4PF_6 led to the formation of 16-electron iridium(III) complexes **Ir3−Ir8** and 18-electron ruthenium(II) complexes **Ru3−Ru7** as the PF_6^- salts in 46−57% isolated yields (Scheme 2c). Thus, NH_4PF_6 served only as a reagent for anion exchange in this reaction. All of these new complexes were air-stable and highly soluble in commonly used solvents like acetonitrile, dimethyl sulfoxide (DMSO), methanol and dichloromethane but poorly soluble in aqueous solution. Therefore, nontoxic amounts of DMSO were used in the subsequent biological experiments to assist dissolution. The purity and identity of these complexes have been determined through spectroscopic analysis (^{1}H, $^{13}C\{^1H\}$ NMR, and mass spectra) and CHN elemental analysis. The ^{1}H NMR spectra of 16-electron iridium(III) complexes showed two characteristic peaks corresponding to the proton of the N*H* group (chemical shift: 11.80−15.31 ppm) and the C*H*=N group (chemical shift: 8.68−9.32 ppm). However, the signal for the N*H* group of **Ir3** was not observed. In the case of 18-electron ruthenium(II) complexes, the characteristic peak corresponding to C*H*=N was at 8.30−8.55 ppm, which was similar to the 16-electron iridium(III) complexes. The signals of each proton of the NH_2 group in **Ru1** and **Ru2** are displayed separately. One peak corresponding to the NH_2 group was at 10.13 and 10.47 ppm, while the

https://doi.org/10.1021/acs.inorgchem.3c03471
Inorg. Chem. 2023, 62, 21379−21395

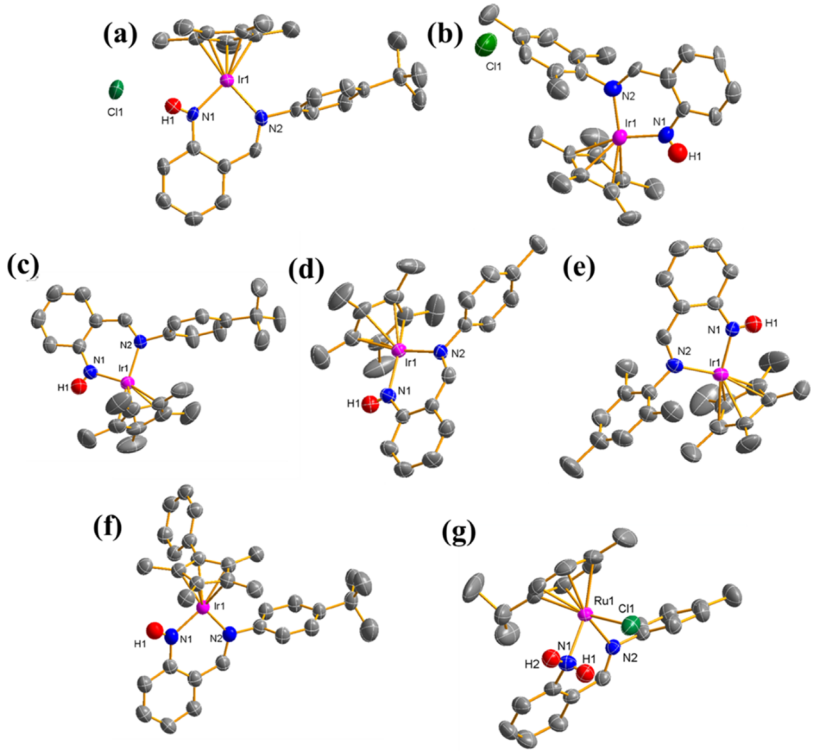

Figure 1. X-ray crystal structures of complexes **Ir1** (a), **Ir2** (b), **Ir3** (c), **Ir4** (d), **Ir6** (e), **Ir8** (f), and **Ru4** (g) with the thermal ellipsoids drawn at the 50% probability level. The hydrogen atoms in all of these complexes and PF_6^- in **Ir3**, **Ir4**, **Ir6**, **Ir8**, and **Ru4** have been omitted for clarity.

other peak was at 4.95−5.01 ppm. However, only one peak, corresponding to one of the exchangeable NH_2 protons, was observed in the ^{1}H NMR spectra of **Ru3**−**Ru7**. In the ^{13}C{^{1}H} NMR spectra, the characteristic peaks of these complexes were at 160.44−164.29 ppm (Figures S4, S6, S8, S10, S12, S14, S16, S18, S20, S22, S24, S26, S28, S30 and S32), which were assigned to the imine carbon of the C*H*=N group. Moreover, single-crystal structures were also obtained for some typical complexes.

The molecular structure of **Ir1**−**Ir4**, **Ir6**, **Ir8**, and **Ru4** was confirmed using single-crystal X-ray diffraction analysis, as shown in Figure 1a−g and Tables S1−S2. The iridium(III) complexes **Ir1**−**Ir4**, **Ir6**, and **Ir8** had an unsaturated 16-electron geometry without coordination of chlorine atoms to the metal center, while the ruthenium(II) complex **Ru4** adopted an 18-electron six-coordinated "three-legged piano-stool" geometry with Cl^- as the monodentate labile ligand. The Ir−N1 bonds (1.924 to 1.996 Å) in these 16-electron complexes were shorter than the Ir−N2 bond distances (1.985−2.068 Å). In contrast, the Ru−N1 bond (metal−amine bond: 2.144 Å) in the 18-electron complex **Ru4** was longer than that of Ru−N2 bond distance (metal−imine bond: 2.114 Å). This difference in bond lengths may originate from the different coordination modes between the iridium(III) and ruthenium(II) complexes. The distances of the C−N1 single bond (1.343−1.445 Å) on the six-membered chelating ring of these complexes were slightly longer than those of the C=N2 bond (1.292−1.404 Å) on the six-membered chelating ring. The variation of counteranions from Cl^- to PF_6^- had little impact on the bond distances and angles of these complexes (**Ir1** vs **Ir3**; **Ir2** vs **Ir6**).

Further, our interest in 16-electron five-coordinated ruthenium(II) complexes prompted us to perform the deprotonation reaction of these 18-electron amine−imine ruthenium(II) complexes. The reaction of 18-electron complex **Ru3** with a slight excess of deprotonating agent NaOAc in the mixture of dichloromethane and methanol at room temperature afforded 16-electron complex **Ru8** in 95% isolated yield (Scheme 3). The molecular structure of **Ru8** was determined

Scheme 3. Synthesis of 16-Electron Ru8 in the Presence of Base NaOAc

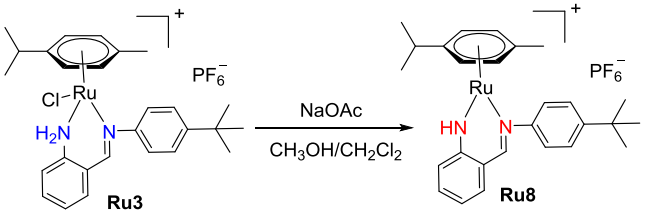

by ^{1}H, ^{13}C{^{1}H} NMR (Figures S33 and S34), elemental analysis, mass spectrum (Figures S51), and X-ray crystallography (Figure 2). A frequency shift of 13.28 ppm was observed in the ^{1}H NMR spectra of **Ru8** due to the proton of the N*H* group. **Ru8** adopted a 16-electron five-coordinated geometry and no monodentate labile group Cl^- was bound to the metal center (Figure 2). In contrast to the 18-electron six-coordinated ruthenium(II) complex **Ru4**, the Ru−N1 bond (metal−amine bond: 1.943 Å) in the 16-electron complex **Ru8** was shorter than the Ru−N2 bond distance (metal−imine bond: 2.014 Å). However, this result was consistent with the 16-electron iridium(III) complexes in this system, further supporting the key role of coordination mode in determining the metal−nitrogen bond lengths.

2.2. Absorption and Emission Spectroscopy. The UV−vis absorption spectra of **Ir1**−**Ir8** (Figure 3a) and **Ru1**−**Ru8** (Figure 3b) were recorded at 37 °C in methanol solutions. The

https://doi.org/10.1021/acs.inorgchem.3c03471
Inorg. Chem. 2023, 62, 21379−21395

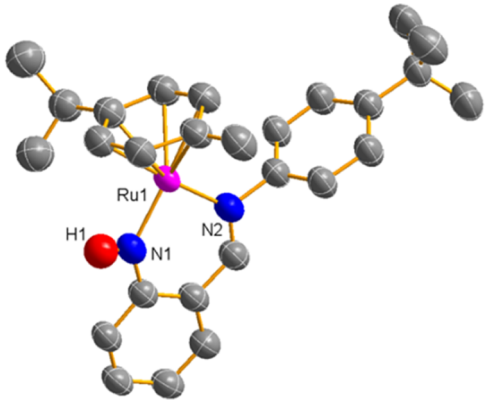

Figure 2. X-ray crystal structures of complex **Ru8** with the thermal ellipsoids drawn at the 50% probability level. The hydrogen atoms and PF_6^- have been omitted for clarity.

iridium(III) complexes **Ir1**−**Ir8** exhibited a relatively sharp band with a maximum in the range of 265−294 nm. In addition, two broad and less intense bands with maxima at approximately 320 and 406 nm were observed. Similarly, the ruthenium(II) complexes **Ru1**−**Ru8** displayed a sharp band with a maximum at 285−320 nm, as well as two very weak and broad bands with a maximum at approximately 370 and 490 nm, respectively. These absorption bands that fall below 320 nm were associated with $\pi-\pi^*$ ligand-centered spin-allowed transitions. Additionally, the absorption bands between 320 and 490 nm can be attributed to spin-allowed charge transfer from metal to ligand. Notably, the absorption behavior of these complexes was similar to that of earlier reported half-sandwich iridium(III) and ruthenium(II) complexes.[48−51]

Upon excitation at λ_{ex} = 398 nm, **Ir1**−**Ir8** (Figure 3c) and **Ru1**−**Ru8** (Figure 3d) exhibited emission maxima (λ_{em}) ranging from 465 to 477 nm (**Ir1**: 471 nm, **Ir2**: 476 nm, **Ir3**: 477 nm, **Ir4**: 472 nm, **Ir5**: 470 nm, **Ir6**: 465 nm, **Ir7**: 472 nm, **Ir8**: 475 nm, **Ru1**: 472 nm, **Ru2**: 471 nm, **Ru3**: 472 nm, **Ru4**: 465 nm, **Ru5**: 468 nm, **Ru6**: 468 nm, **Ru7**: 470 nm, **Ru8**: 472 nm) at 37 °C in methanol solutions. Overall, the emission spectra of these complexes were insensitive to the change in metal ions, counteranion (Cl^- or PF_6^-), coordination mode (16- or 18-electron), and ligand substituents. The relative emission quantum yields (Φ) of complexes **Ir3**, **Ru3**, and **Ru8**, measured using fluorescein as the standard, were relatively low in ethanol solutions. Specifically, **Ir3** had a quantum yield of 0.148, **Ru3** had a quantum yield of 0.084, and **Ru8** had a quantum yield of 0.065. The average lifetimes of **Ir3**, **Ru3**, and **Ru8** were 2.85, 1.91, and 1.97 ns, respectively (Figure S52), suggesting that these complexes were fluorescent. It should be noted that the similar weakly fluorescent behavior has also

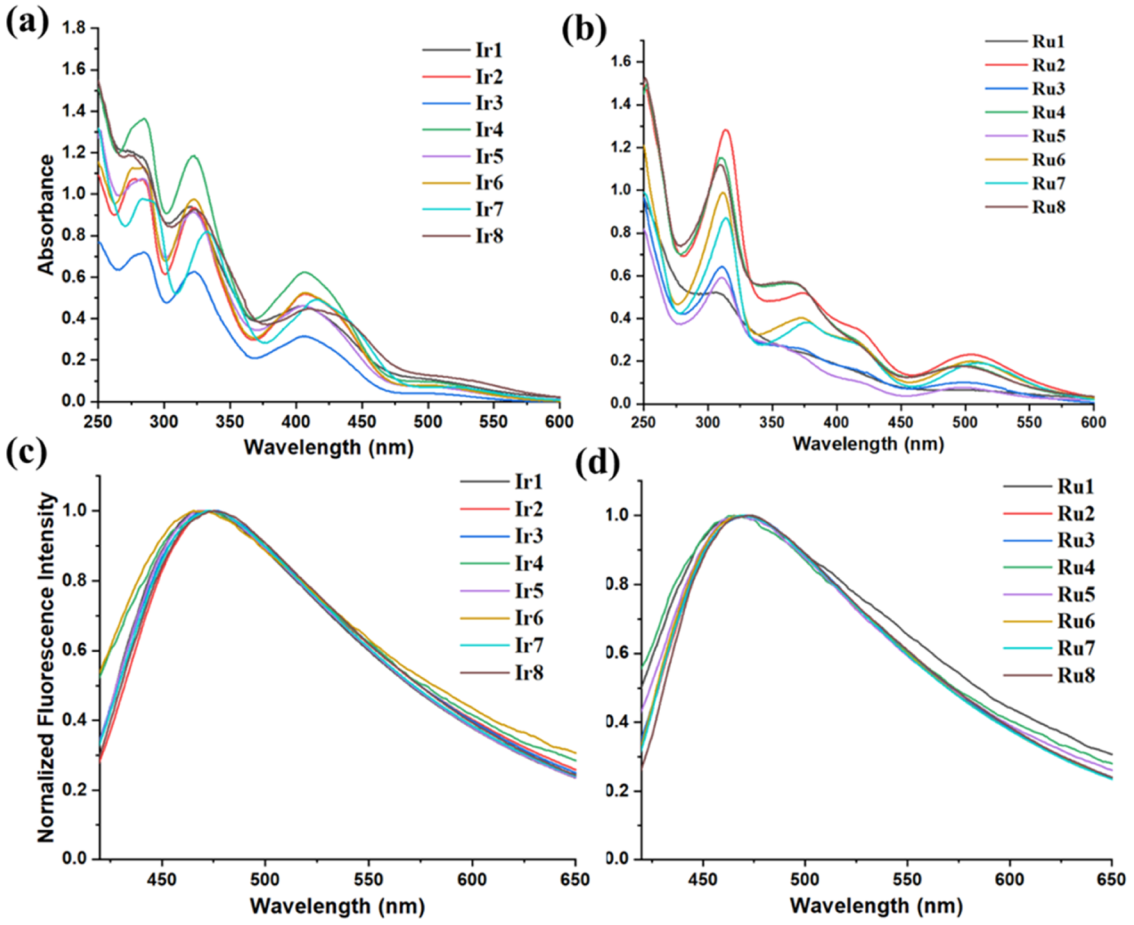

Figure 3. (a) UV−visible absorbance spectra of complexes **Ir1**−**Ir8** (20 μM) in methanol solutions at 37 °C. (b) The UV−visible absorbance spectra of complexes **Ru1**−**Ru8** (20 μM) in methanol solutions at 37 °C. (c) Normalized emission spectra of complexes **Ir1**−**Ir8** (20 μM) in methanol at 37 °C (**Ir1**−**Ir8**: λ_{ex} = 398 nm). (d) Normalized emission spectra of complexes **Ru1**−**Ru8** (20 μM) in methanol at 37 °C (**Ru1**−**Ru8**: λ_{ex} = 398 nm).

https://doi.org/10.1021/acs.inorgchem.3c03471
Inorg. Chem. 2023, 62, 21379−21395

Table 1. IC_{50} Values of Complexes Ir1−Ir8 and Ru1−Ru8 Tested toward Cancer and Normal Cell Lines and Comparison with Cisplatin

	IC_{50} (μM)					
complexes	A549	A549/DDP	HeLa	HepG2	BEAS-2B	SI[a]
Ir1	11.17 ± 0.06	13.06 ± 0.41	10.31 ± 0.25	16.29 ± 0.09	23.36 ± 0.24	2.1
Ir2	11.01 ± 0.22	12.98 ± 0.16	10.48 ± 0.13	15.35 ± 0.16	23.04 ± 0.17	2.1
Ir3	10.75 ± 0.14	12.23 ± 0.13	9.89 ± 0.37	14.83 ± 0.06	22.66 ± 0.21	2.1
Ir4	10.01 ± 0.16	11.21 ± 0.19	9.74 ± 0.32	14.27 ± 0.15	22.89 ± 0.06	2.3
Ir5	8.61 ± 0.05	11.31 ± 0.25	9.02 ± 0.18	12.16 ± 0.31	21.32 ± 0.25	2.5
Ir6	8.34 ± 0.16	10.37 ± 0.11	8.85 ± 0.06	11.98 ± 0.24	21.84 ± 0.32	2.6
Ir7	6.32 ± 0.09	8.64 ± 0.09	7.15 ± 0.03	9.88 ± 0.32	20.25 ± 0.54	3.2
Ir8	5.41 ± 0.19	7.23 ± 0.06	6.26 ± 0.08	9.29 ± 0.14	20.17 ± 0.34	3.7
Ru1	8.29 ± 0.10	9.94 ± 0.07	8.94 ± 0.31	11.34 ± 0.18	22.65 ± 0.31	2.7
Ru2	8.65 ± 0.06	9.52 ± 0.03	8.65 ± 0.10	11.87 ± 0.25	22.18 ± 0.09	2.6
Ru3	7.41 ± 0.05	8.23 ± 0.14	7.98 ± 0.13	10.36 ± 0.26	21.17 ± 0.08	2.9
Ru4	6.91 ± 0.24	8.14 ± 0.22	6.88 ± 0.06	9.59 ± 0.09	21.51 ± 0.22	3.1
Ru5	6.64 ± 0.07	8.31 ± 0.15	6.25 ± 0.31	9.29 ± 0.06	20.98 ± 0.11	3.2
Ru6	6.52 ± 0.03	8.25 ± 0.19	6.56 ± 0.13	10.67 ± 0.29	21.89 ± 0.17	3.4
Ru7	6.26 ± 0.06	8.47 ± 0.08	6.05 ± 0.22	11.78 ± 0.30	21.78 ± 0.36	3.5
Ru8	9.12 ± 0.15	10.16 ± 0.12	9.89 ± 0.13	12.98 ± 0.33	22.18 ± 0.28	2.4
Cisplatin	23.96 ± 0.23	>100	7.55 ± 0.06	22.7 ± 0.58	28.27 ± 0.28	1.2

[a]SI: selectivity index represents the IC_{50} ratio of BEAS-2B normal cells to A549 cancer cells.

been observed in some other reported half-sandwich iridium(III) and ruthenium(II) complexes.[43,44,49] Probably, the exploration of MoAs through bioimaging can be facilitated by the photoluminescence characteristic of these complexes.

2.3. Solution Stability and Reactivity. To investigate the stability of the complexes in an aqueous solution, **Ir3**, **Ir4**, **Ru1**, **Ru3**, **Ru5**, and Ru8 were monitored at 37 °C in 85% DMSO-d_6/15% phosphate-buffered saline (PBS) (v/v, pH ≈ 7.2, prepared from D_2O) solutions by ^1H NMR (Figures S53−S58). No additional peaks were observed in the ^1H NMR spectra for 24 h, and the assignment of protons was completely in agreement with their molecular structures, suggesting that no decomposition or ligand dissociation occurred and these complexes had sufficient stability under test conditions.

The stability of these complexes had also been estimated at 37 °C in 20% DMSO/80% PBS (v/v, pH ≈ 7.2, prepared from H_2O) using UV−vis spectroscopy at different time intervals over a period of 8 h. Negligible or minor changes were observed in the absorption spectra of these complexes (Figures S59 and S60), evidencing their stability in diluted solutions with a high content of water, which was also in agreement with the NMR analysis. However, the absorption intensity in the spectra of 18-electron complexes **Ru1** and **Ru2** changed, while no obvious shift for the absorption bands was observed, suggesting the hydrolysis of metal−Cl bond (Cl^-/H_2O exchange) in **Ru1** and **Ru2**, which were consistent with some reported ruthenium(II) complexes containing the monodentate labile chloride ligand.[52−54] Notably, the hydrolysis of metal−Cl bond generally represented an activation step for a large number of reported anticancer complexes.[55,56] Half-lives ($t_{1/2}$) and hydrolysis rate constants (k) of **Ru1** ($t_{1/2}$ = 129 min, k = 0.00538 min^{-1}) and **Ru2** ($t_{1/2}$ = 176 min, k = 0.00394 min^{-1}) were calculated by fitting the absorption difference to pseudo-first-order kinetics. Hence, the complexes in this system were fairly stable or underwent a relatively slow hydrolysis rate in comparison with the reported half-sandwich iridium(III) and ruthenium(II) complexes chelating N,N donors.[24,54,56] Consequently, these complexes can be employed to proceed with further anticancer studies under aqueous conditions.

Some rarely reported half-sandwich 16-electron iridium(III) and ruthenium(II) complexes have been shown to react with two-electron donors to form the stable 18-electron compounds.[57,58] When PPh_3, CH_3CN, or CO was added into an NMR tube containing a $CDCl_3$ solution of 16-electron complexes **Ir6**, **Ir7**, and **Ru8**, no additional peaks in the ^1H NMR spectra of **Ir6**, **Ir7**, and **Ru8** were detected over a period of 24 h (Figures S61−S65), indicating that the 16-electron iridium(III) and ruthenium(II) complexes in this system exhibited inert reactivity toward two-electron donors, such as PPh_3, CH_3CN, and CO. The inert reactivity of these complexes was also consistent with their above-mentioned stable nature in aqueous solutions.

2.4. Cytotoxicity. With cisplatin as the standard control, the cytotoxicity of **Ir1−Ir8** and **Ru1−Ru8** toward A549 lung cancer cells, cisplatin-resistant A549/DPP cells, cervical carcinoma HeLa cells, human hepatocellular liver carcinoma HepG2 cells, and noncancerous BEAS-2B cells was evaluated using MTT assay (Table 1). Neither the bimetallic precursors nor the free amine−imine ligands displayed cytotoxicity against A549 and HeLa cancer cells (IC_{50} > 100 μM) (Table S3). However, all of the amine−imine complexes **Ir1−Ir8** and **Ru1−Ru8** showed strong cytotoxicity toward A549, A549/DDP, HeLa, and HepG2 cells with IC_{50} values in a narrow range of 5.41−11.17, 7.23−13.06, 6.05−10.48, and 9.29−16.29 μM, respectively, which were comparable to or even better than commercial cisplatin. As a result, the anticancer efficiency of these complexes arose from the chelation of the free ligands with the iridium(III) or ruthenium(II) ion. Specifically, these complexes were approximately 2−4 times more potent than cisplatin toward A549 cancer cells (5.41−11.17 vs 23.96 μM). Interestingly, all of these iridium(III) and ruthenium(II) complexes also showed high cytotoxicity against cisplatin-resistant A549/DPP cells with IC_{50} values in the range 7.23−13.06 μM, suggesting the different MoAs of these complexes with cisplatin. The trend in potency was maintained across the different cell lines, indicating that the MoAs were not

https://doi.org/10.1021/acs.inorgchem.3c03471
Inorg. Chem. 2023, 62, 21379−21395

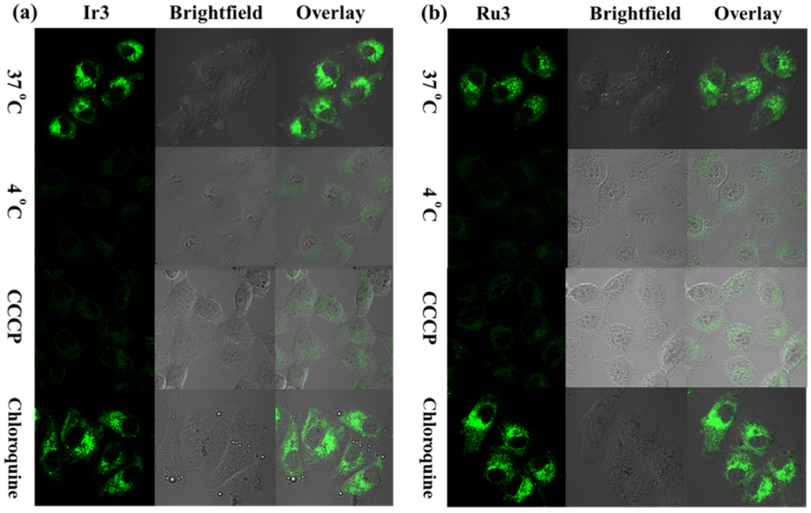

Figure 4. (a) Effects of temperatures (37 or 4 °C), chloroquine (50 μM), and CCCP (50 μM) on cellular uptake of **Ir3** (2 μM). Scale bar: 20 μm, λ_{ex} = 405 nm, λ_{em} = 430−490 nm. (b) Effects of temperatures (37 or 4 °C), chloroquine (50 μM), and CCCP (50 μM) on cellular uptake of **Ru3** (2 μM). Scale bar: 20 μm, λ_{ex} = 405 nm, λ_{em} = 430−490 nm.

dependent on the cell type. Notably, the variation of metal center (Ir vs Ru), counteranion (Cl^- vs PF_6^-), coordination mode (16-electron vs 18-electron) and ligand substitution showed little impact on the cytotoxicity of these complexes. However, the introduction of the extended lipophilic phenyl substituents on the η^5-Cp^x ring of the iridium(III) complexes led to the increase of the cytotoxicity toward all of the cell lines (**Ir3** vs **Ir8**), which was in agreement with the increasing trend of the previously reported N,N-chelating half-sandwich iridium(III) complexes bearing bpy or α-diimine ligands.[24,34] Moreover, these complexes showed a certain selectivity toward A549 over BEAS-2B cells with the values of selectivity index ranging from 2.1 to 3.7. However, all of the iridium(III) and ruthenium(II) complexes in this system were still active toward noncancerous BEAS-2B cells.

2.5. Interaction with Nucleobases. The potential binding to the DNA model nucleobase 9-methyladenine (9-MeA) of **Ir4**, **Ru1**, **Ru2**, **Ru3**, **Ru5**, and **Ru8** was evaluated using ^{1}H NMR spectroscopy in a solution of 85% DMSO-d_6/15% D_2O (Figures S66−S71). No coordination reaction occurred between 9-MeA and these complexes over a period of 24 h. In addition, the formation of nucleobase adducts was also not detected via mass spectrometry. Therefore, DNA binding may not be the primary MoAs for these amine−imine iridium(III) and ruthenium(II) complexes, which was further supported by their low colocalization efficiency in the nucleus (see Section 2.8).

2.6. Protein Binding Studies. It is important to understand the interactions between anticancer agents and proteins in cells. Serum albumin (SA) is a major protein in blood plasma that helps transport and metabolize complexes. In this study, bovine serum albumin (BSA) was used as a substitute for human serum albumin (HSA) because it is structurally similar and easier to obtain. The binding potency of complexes **Ir3**, **Ir4**, **Ru4**, and **Ru8** with BSA was evaluated by UV−vis absorption and fluorescence spectra (Figure S72). Both the reference and sample cuvettes were treated with the corresponding complexes to eliminate self-absorption. The fluorescence characteristic of BSA is usually due to two protein residues called tyrosine (Tyr) and tryptophan (Trp). These residues contain aromatic amino acids that are sensitive to changes in their surroundings. When small-molecule complexes bind to these residues, fluorescence emission can be suppressed. The increase in the concentration of the complexes caused a decrease and red shift in the absorption peak at 229 nm, which may be due to the effect of inducing α-helix perturbations and the impact of polar solvents.[59−64] In addition, a progressive increase without any shift was observed in the absorption peak of BSA at 276 nm for these complexes, suggesting a kind of tiny variation of microenvironment of aromatic amino acid residues (Tyr and Trp) in BSA.[65,66] The fluorescence intensity of BSA showed a regular decline at 353 nm with an increase in the concentration of **Ir3**, **Ir4**, **Ru4**, and **Ru8**, suggesting that these complexes interacted with BSA through a static quenching mode.[67]

Synchronous fluorescence spectrometry is a valuable tool for understanding the conformational changes that occur in BSA after adding complexes. When the wavelength interval remains stable at either 15 or 60 nm, synchronized fluorescence could reveal the characteristic information on Trp or Tyr residues in BSA. The emission wavelength of Trp decreased at 276 nm ($\Delta\lambda$ = 60 nm) with a red shift of 4 nm, while the emission wavelength of Tyr decreased at 287 nm ($\Delta\lambda$ = 15 nm) with a minor red shift of 1 nm (Figure S73). These observations suggested that **Ir3**, **Ir4**, **Ru4**, and **Ru8** primarily affected the Trp microregion's conformation when binding to BSA.

2.7. Cellular Uptake Pathway. Since these complexes displayed fluorescence characteristics, laser confocal microscopy was used to determine how these complexes entered the cells. According to the observation of confocal microscopy images for the selected 16-electron **Ir3** and 18-electron **Ru3** at λ_{ex} = 405 nm at 37 °C, it seemed that **Ir3** and **Ru3** were able to effectively enter A549 cells after 1 h of incubation, as shown by the presence of punctate green fluorescence in the cytoplasm (Figure 4a,b). It is well-known that small-molecule drugs can penetrate cells through either the energy-dependent or energy-independent pathway.[68] In comparison with the control group incubated at 37 °C, the fluorescence intensity of A549 cells decreased significantly when incubated with **Ir3** or **Ru3** at a low temperature (4 °C) or pretreated with carbonyl cyanide 3-chloro-phenylhydrazone (CCCP, a metabolic inhibitor). These results indicated that the cellular uptake mechanism for **Ir3**

https://doi.org/10.1021/acs.inorgchem.3c03471
Inorg. Chem. 2023, 62, 21379−21395

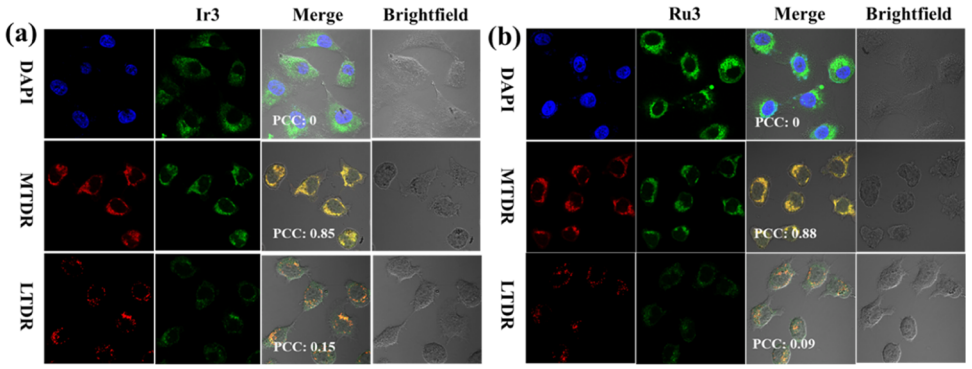

Figure 5. Determination of intercellular localization of **Ir3** (a) and **Ru3** (b) by confocal microscopy. A549 cells were incubated with **Ir3** and **Ru3** (2 μM) for 1 h at 37 °C and then coincubated with DAPI (1 μg/mL), MTDR (500 nM), or LTDR (75 nM) for 1 h, respectively. **Ir3** and **Ru3**, λ_{ex} = 405 nm, λ_{em} = 460−520 nm; DAPI, λ_{ex} = 345 nm, λ_{em} = 410−455 nm; MTDR, λ_{ex} = 644 nm, λ_{em} = 660−720 nm; LTDR, λ_{ex} = 594 nm, λ_{em} = 600−660 nm. Scale bar: 20 μm. The green, red, and blue fluorescence represent **Ir3** and **Ru3**, mitochondria or lysosome, and nucleus, respectively.

and **Ru3** was energy-dependent. Further, there was no significant difference in the intracellular fluorescence intensity between A549 cells treated with the endocytosis inhibitor chloroquine and the untreated cells, indicating that endocytosis was not responsible for the uptake pathway of **Ir3** and **Ru3**.

2.8. Cellular Localization. In order to evaluate the possible cellular target of these complexes, intracellular localization analysis in different organelles was also measured by using confocal microscopy (Figure 5a,b). 4,6-Diamino-2-phenyl indole (DAPI), Mito Tracker Red CM-H2XRos (MTDR), and LysoTracker Red DND-99 (LTDR) were employed as the nucleus and mitochondrial and lysosome probes, respectively. The A549 cells were dual-stained with these organelle-specific probes and **Ir3** or **Ru3**. After treatment for 1 h, distinct green fluorescence in the cytoplasm was detected, suggesting that **Ir3** and **Ru3** effectively penetrated A549 cells. **Ir3** and **Ru3** showed a negligible degree of merging with DAPI or LTDR. The Pearson correlation coefficient (PCC) values for DAPI and LTDR were both very low (**Ir3**: PCC = 0 for DAPI and PCC = 0.15 for LTDR; **Ru3**: PCC = 0 for DAPI and PCC = 0.09 for LTDR), which suggested that these complexes were not effectively localized in the nucleus and lysosome. However, these complexes can effectively accumulate in mitochondria with high PCC values (**Ir3**: PCC = 0.85; **Ru3**: PCC = 0.88). These results indicated that **Ir3** and **Ru3** had a selective localization in the mitochondria, and the cytotoxicity of these complexes may be caused by mitochondria-mediated cell death. Since cancer cells contained more mitochondria than normal cells, they were much more sensitive to the disruption of mitochondria than normal cells, which may lead to certain anticancer selectivity (SI: 2.1−3.7) of the complexes in this system. Notably, the high positive ζ-potential of **Ir3** (46.58 ± 0.19) and **Ru3** (50.93 ± 0.32) was observed (Figure S74), which could contribute to targeting mitochondria with negative charges on the surface after entering the cytosol. Since the mitochondria-targeting was likely associated with the hydrophobicity of these complexes, the distribution coefficient, i.e., log P value of the selected complexes **Ir3**, **Ru3**, and **Ru8**, was also measured using the shake-flask method. These complexes showed almost equal log P values ranging from 1.23 to 1.49 (**Ir3**: 1.49; **Ru3**: 1.23; **Ru8**: 1.33), suggesting high hydrophobicity. The small change in the hydrophobicity of these complexes was also consistent with their similar cytotoxicity toward various cancer cells. Hence, the high hydrophobicity of these complexes may also contribute to the mitochondria-targeting.

2.9. Mitochondrial Membrane Depolarization. Since these complexes could selectively accumulate in the mitochondria, the possible influence of these complexes on the functional status of mitochondria was also investigated. The maintenance of the mitochondrial membrane potential (MMP, $\triangle\psi_m$) is essential for mitochondrial integrity and bioenergetics function. The loss of MMP is often regarded as an early event in the mitochondrion-mediated apoptosis pathway. Thus, analysis of $\triangle\psi_m$ in A549 cancer cells was performed after exposure to **Ir3** or **Ru3** at concentrations of 0.5, 1, and 2 × IC_{50}. The changes in MMP can be detected by JC-1 staining using flow cytometry. A decrease in the ratio of the red to green fluorescence intensity can be observed when mitochondrial depolarization occurred. The MMP in A549 cells displayed a significant decrease compared with the untreated cells. The concentration-dependent mitochondrial dysfunction in A549 cells was also observed for both **Ir3** and **Ru3**. When the concentration of **Ir3** and **Ru3** was increased from 0.5 × IC_{50} to 2 × IC_{50}, the percentage of A549 cells suffering mitochondrial membrane depolarization showed an increase from 34.47 and 13.93% to 57.17 and 42.16%, respectively (Figure 6a,b). These results were consistent with the aforementioned mitochondria-targeting behavior of **Ir3** and **Ru3**. Therefore, these complexes could exert their anticancer actions by targeting mitochondria and inducing mitochondrial dysfunction.

2.10. Cellular ROS Determination. The production of intracellular reactive oxygen species (ROS) is strongly associated with mitochondria.[69−71] Previous studies have shown that dysfunctional mitochondria are unable to effectively regulate ROS production, resulting in elevated oxidative stress in cancer cells.[26,72] It has been reported that anticancer complexes that produce high levels of ROS can disturb the redox balance in cells, thus leading to cell apoptosis and damage.[70,73,74] Therefore, we also became interested in investigating the effect of these complexes on intracellular ROS levels in A549 and cisplatin-resistant A549/DPP cancer cells. The total ROS levels induced by the typical complexes **Ir3** and **Ru3** at the concentrations of 0.5, 1, and 2 × IC_{50} were measured by fluorescence microscopy after staining with the probe DCFH-DA (Figures 7a−c, S75, and S76). Compared to the control cells, the treated A549 cells with complexes **Ir3** and **Ru3** showed a concentration-dependent increase in intra-

https://doi.org/10.1021/acs.inorgchem.3c03471
Inorg. Chem. 2023, 62, 21379−21395

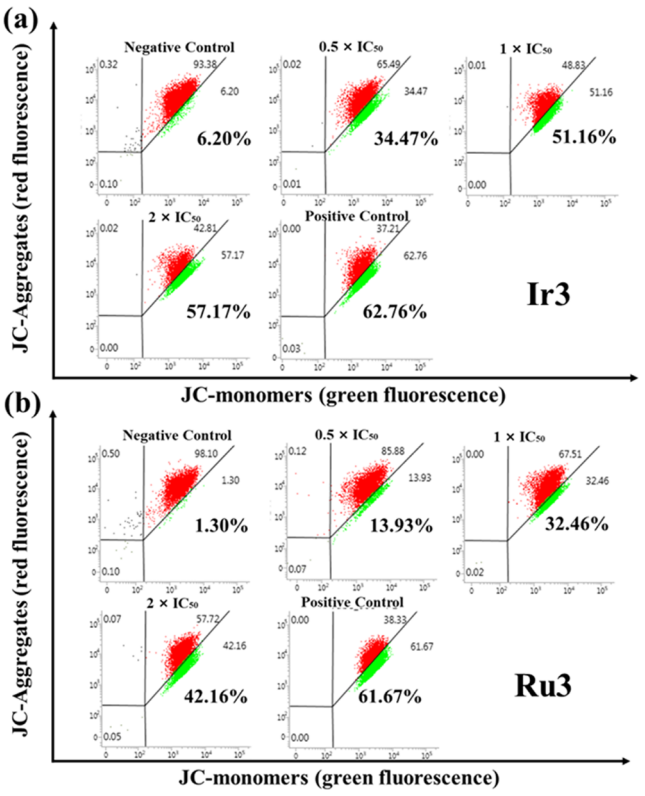

Figure 6. Changes in the mitochondrial membrane potential of A549 cancer cells induced by **Ir3** (a) and **Ru3** (b).

cellular ROS levels (Figure 7a,b), which indicated that ROS generation played a key role in the induction of cell death for these complexes. Notably, the ROS levels in cisplatin-resistant A549/DPP cells treated with **Ir3** also increased in a concentration-dependent manner (Figure 7c). Moreover, the fluorescence intensity in A549 cells, which is proportional to the ROS levels, was comparable to that in A549/DDP cells under the same concentrations of **Ir3**. Thus, the overcoming of cisplatin resistance for these complexes can be attributed to the redox mechanism arising from ROS overproduction.

Many reported half-sandwich iridium(III) and ruthenium(II) complexes can produce ROS by the catalytic oxidation of nicotinamide adenine dinucleotide (NADH) to NAD^+.[28,75−77] As a result, the reaction of **Ir3**, **Ru3**, and **Ru8** (1 equiv) with NADH (ca. 100 equiv) in 10% MeOH/90% H_2O (v/v) was monitored within 8 h by UV−vis spectroscopy at 25 °C (Figure S77). The decrease in the absorption intensity of the NADH band (339 nm) can be used to determine the conversion of NADH to NAD+. The calculated turnover numbers (TONs) of **Ir3** (5.47), **Ru3** (9.81), and **Ru8** (6.43) were quite similar, which was also in agreement with their small change in the ROS generation and cytotoxicity. Thus, the catalytic conversion of NADH to NAD^+ for these amine−imine iridium(III) and ruthenium(II) complexes may also be one of the mechanism actions for the generation of ROS.

2.11. Apoptosis. One potential goal of anticancer agents is to target cancer cells and trigger their death through the apoptosis pathway. It has been found that the induction of apoptosis was closely related to the disruption of redox balance.[78,79] As a result, **Ir3** and **Ru3** were also selected to verify whether these complexes can induce cell apoptosis by using the dual-staining annexin V/PI assay. A549 or A549/DPP cells were incubated with **Ir3** or **Ru3** at the concentration of 0.25, 0.5, and 1 × IC_{50} for 48 h and then detected by flow cytometry (Figure 8a−c). In comparison to the control group, an increase in the percentage of both early and late apoptotic cells was observed for complexes **Ir3** and **Ru3**. When **Ir3** and **Ru3** were at 1 × IC_{50} concentration, a total of 52.5% (31.7% early apoptosis and 20.8% late apoptosis) and 29.7% (9.60% early apoptosis and 20.1% late apoptosis) of A549 cells underwent apoptosis, respectively (Figure 8a,b). In addition, the late apoptotic cell populations increased in a concentration-dependent manner for **Ru3**, although the increase of the early apoptotic cell populations was insignificant when the concentrations increased from 0.5 to 1 × IC_{50}. Moreover, **Ir3** showed a concentration-dependent increase in both early and late apoptotic cell populations. A similar trend was also observed in the cisplatin-resistant A549/DDP cells treated with **Ir3**, which was basically identical to that in A549 cells (Figure 8c). These observations were correlated with the above-mentioned loss of MMP and ROS production of **Ir3** and **Ru3** toward A549 and A549/DPP cells and indicated that these iridium(III) and ruthenium(II) complexes can induce cell death via the apoptotic pathway.

2.12. Cell Cycle Arrest. The cell cycle arrest may be affected by apoptotic signals and was also associated with the acceleration of cell apoptosis. Some transition metal-based anticancer complexes were reported to induce cell apoptosis by blocking the cell cycle.[80,81] The effects of **Ir3** and **Ru3** on cell cycle arrest in A549 cancer cells were also explored by using flow cytometry (Figures 9, S78, and S79). Treatment of A549 cells with **Ir3** or **Ru3** at the concentrations of 0.25 × IC_{50} and

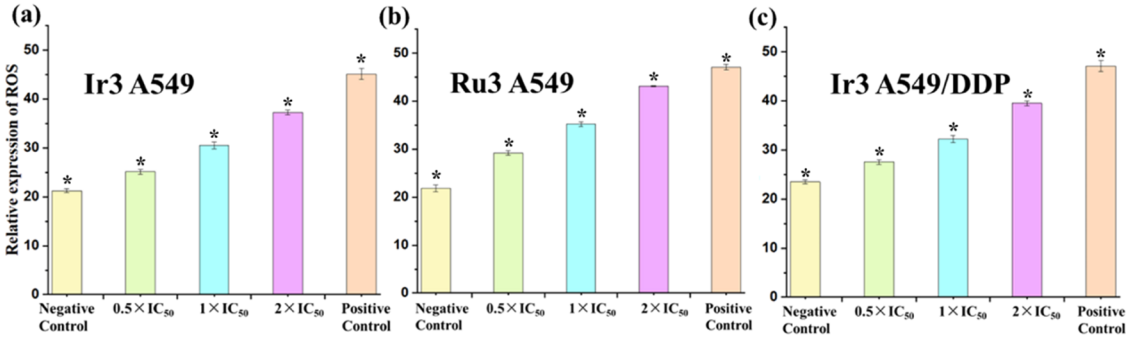

Figure 7. Analysis of ROS levels by fluorescence microscopy after A549 cells were treated with **Ir3** (a) or **Ru3** (b) for 24 h at 37 °C and A549/DDP cells were treated with **Ir3** (c) for 24 h at 37 °C and stained with DCFH-DA. Data are quoted as mean ± standard deviation (SD) of three replicates. *p*-Values were calculated after a test against the negative control data, $*p < 0.05$.

https://doi.org/10.1021/acs.inorgchem.3c03471
Inorg. Chem. 2023, 62, 21379−21395

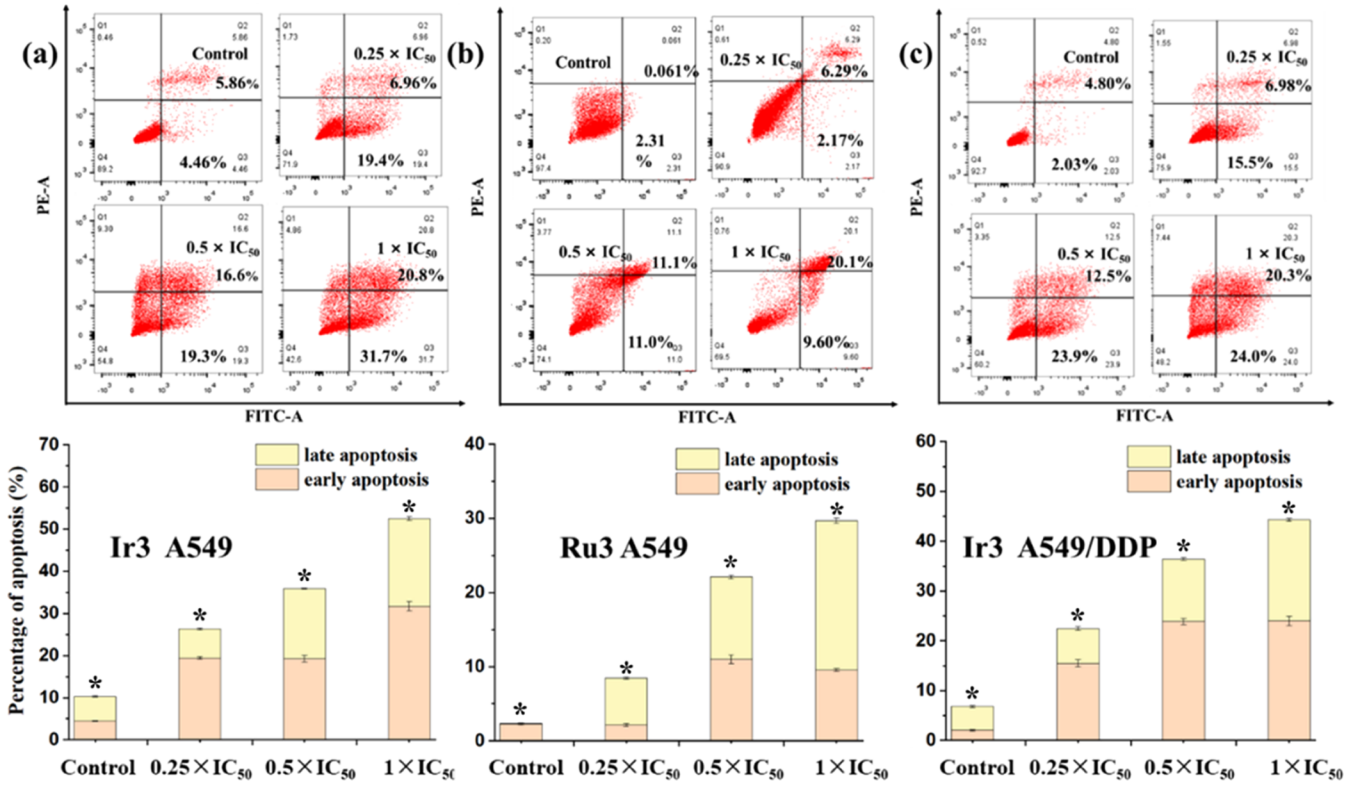

Figure 8. (a) Apoptosis analysis and the corresponding histograms of apoptosis analysis for A549 cells after 48 h of exposure to **Ir3** at 37 °C. (b) Apoptosis analysis and the corresponding histograms of apoptosis analysis for A549 cells after 48 h of exposure to **Ru3** at 37 °C. (c) Apoptosis analysis and the corresponding histograms of apoptosis analysis for A549/DDP cells after 48 h of exposure to **Ir3** at 37 °C. Determined by flow cytometry using annexin V-FITC vs PI staining. Data are quoted as mean ± SD of three replicates. *p*-Values were calculated after a test against the negative control data, $*p < 0.05$.

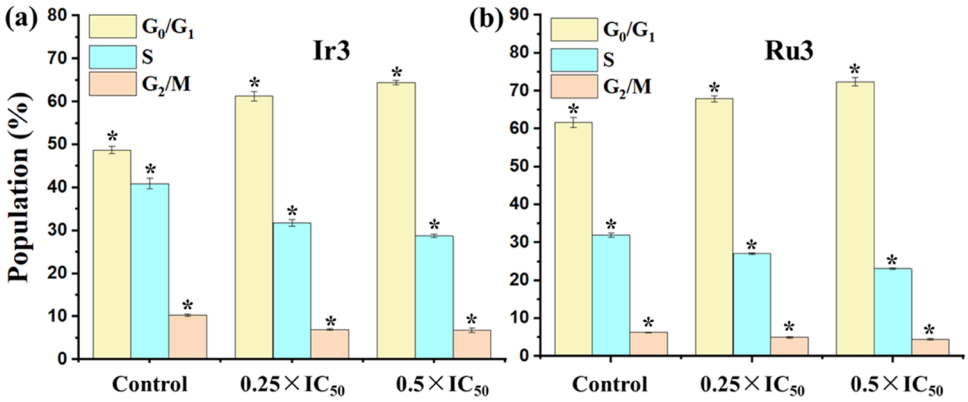

Figure 9. Flow cytometry data for the cell cycle distribution of A549 cancer cells exposed to **Ir3** (a) and **Ru3** (b) for 24 h. The concentrations used were 0.25 × IC_{50} and 0.5 × IC_{50}. Cell staining for flow cytometry was carried out using PI/RNase. Data are quoted as mean ± SD of three replicates. *p*-Values were calculated after a test against the negative control data, $*p < 0.05$.

0.5 × IC_{50} for 24 h led to the concentration-dependent increase of cell population in the G_0/G_1 phase, along with a gradual decrease of cell population in S and G_2/M phases. When **Ir3** and **Ru3** were at the concentration of 0.5 × IC_{50}, the proportion of A549 cells in the G_0/G_1 phase increased by 12.5 and 10.7%, respectively, compared to the untreated group (Figures 9, S78, and S79). As a result, both **Ir3** and **Ru3** induced cell cycle perturbation and arrested the cell cycle in the G_0/G_1 phase.

2.13. Inhibition of Cell Migration. Preventing the spread of cancer cells is highly desired but remains a significant challenge in cancer treatment. A reduction in surface adhesion can cause malignant cells to move away from the original tumor site and travel to other organs.[82,83] Cell migration, invasion, and metastasis were closely related to the degradation of extracellular matrix and different cell adhesion molecules.[84,85] To evaluate the inhibitory effect of **Ir3** and **Ru3** on A549 cancer cell migration, a wound-healing assay was conducted (Figure 10a,b). Compared to the control group (40.5 and 42.5%), the wound closure rate (WCR) of A549 cells incubated with **Ir3** and **Ru3** decreased significantly to 8.1 and 9.0% at 0.5 × IC_{50}, respectively. In addition, both **Ir3** and **Ru3** exhibited a concentration-dependent pattern for the WCR of A549 cells. These results suggested that the amine−imine

https://doi.org/10.1021/acs.inorgchem.3c03471
Inorg. Chem. 2023, 62, 21379−21395

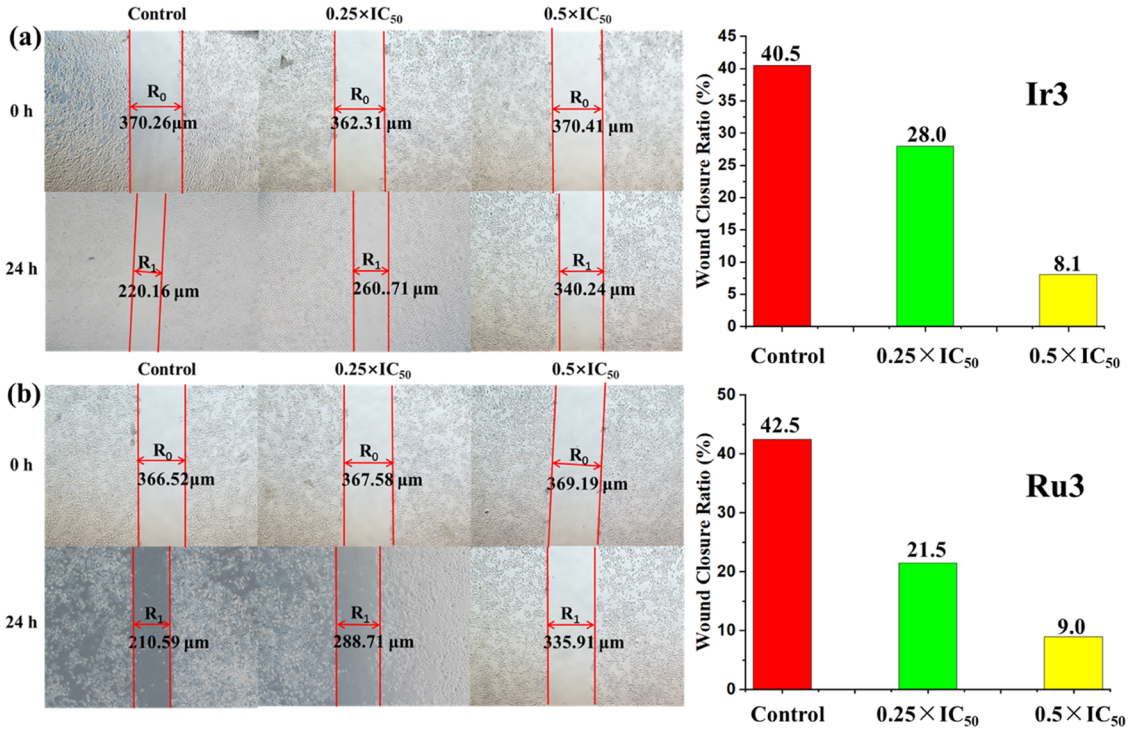

Figure 10. (a) Wound-healing assay and histogram analysis for A549 cells treated with **Ir3** for 24 h. (b) Wound-healing assay and histogram analysis for A549 cells treated with **Ru3** for 24 h. Typical images were taken at 0 and 24 h. The widths of the wounds are indicated with lines (μm). Scale bar: 100 μm. Wound closure rate = $(R_0 - R_1)/R_0 \times 100\%$.

complexes in this system showed the ability to impede the migration of A549 cancer cells.

3. CONCLUSIONS

The anticancer efficacy of 16-electron five-coordinated half-sandwich iridium(III) and ruthenium(II) complexes has been less studied compared to the corresponding 18-electron six-coordinated complexes. In this study, a simple and readily accessible amine−imine ligand was used to successfully prepare a series of potent half-sandwich iridium(III) and ruthenium(II) anticancer complexes. Unsaturated 16-electron iridium(III) and 18-electron ruthenium(II) complexes were formed when the same ligand was used to react with the corresponding chloro-bridged bimetallic metal precursors. Further deprotonation of the 18-electron ruthenium(II) complex **Ru3** by the base NaOAc afforded isolatable 16-electron ruthenium(II) complex **Ru8**. The different coordination modes of these complexes were confirmed by a single-crystal X-ray diffraction analysis. All of the obtained 16-electron complexes were fairly stable in aqueous solution and did not react with two-electron donors, such as CH_3CN, PPh_3, and CO, to form 18-electron adducts. The weak fluorescence for these complexes was verified by spectroscopic studies. All of the 16-electron and 18-electon complexes displayed potent cytotoxicity with the IC_{50} values lower or comparable to cisplatin against A549 cells, HeLa cells, and HepG2 cells. In particular, high cytotoxicity against cisplatin-resistant A549/DDP cells was also observed for these 16-electron and 18-electron complexes, suggesting that they were not cross-resistant with cisplatin. These complexes also displayed a certain selectivity toward A549 cells and BEAS-2B normal cells, although the selectivity index was not high. The anticancer activity and selectivity of these complexes were insensitive to the metal center, counteranion, 16/18-electron coordination mode, and ligand substitution. Microscopic studies ascertained that these complexes entered A549 cells through an energy-dependent pathway and accumulated mainly in mitochondria. The detection of disruption in mitochondrial membrane potential and overproduction of ROS levels suggested that these complexes may induce cell apoptosis (including both early- and late-stage apoptosis) via the mitochondrial pathway. Additionally, the cell cycle arrest in the G_0/G_1 phase and the suppression of the cell migration were also observed in A549 cells treated by these complexes. This type of half-sandwich amine−imine complex may represent a potent platform for the development of redox-based anticancer complexes.

4. EXPERIMENTAL SECTION

General considerations and the synthetic procedure for ligand **L1** are shown in the Supporting Information. The ligands **L2**−**L5** were prepared using literature methods.[45,46] The bimetallic precursors **D1**−**D3** were prepared according to the previously reported procedures.[44,47] The detailed description of biological experiments is also shown in the Supporting Information.

4.1. Synthesis of Complexes. *4.1.1. Synthesis of iridium(III) and ruthenium(II) complexes with Cl^- as counteranion.* The complexes **Ir1**−**Ir2** and **Ru1**−**Ru2** were synthesized by the reaction of bimetallic metal precursors and ligands (molar ratio, 1:2) in CH_2Cl_2/CH_3OH (v/v, ca. 1:1) for 6 h at 25 °C. The solvent was removed under vacuum and the residue redissolved in CH_2Cl_2. Subsequently, *n*-hexane was added to the solution to produce a precipitate, which was subsequently filtered and washed with *n*-hexane. The complexes were subjected to vacuum drying. At room temperature, *n*-hexane was slowly diffused into a CH_2Cl_2 solution to obtain single crystals of **Ir1** and **Ir2**.

Ir1. (57 mg, Yield 46%). ^{1}H NMR (500 MHz, $CDCl_3$) δ 14.73 (s, 1H, N*H*), 9.10 (d, J = 7.9 Hz, 1H), 8.87 (s, 1H, C*H*═N), 7.69 (t, J = 7.2 Hz, 1H), 7.57 (d, J = 8.4 Hz, 2H), 7.47 (d, J = 8.0 Hz, 1H), 7.30 (d, J = 7.4 Hz, 1H), 7.16 (d, J = 8.3 Hz, 2H), 1.79 (s, 15H, Cp*−

https://doi.org/10.1021/acs.inorgchem.3c03471
Inorg. Chem. 2023, 62, 21379−21395

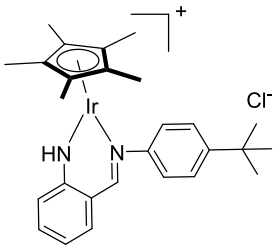

CH_3), 1.42 (s, 9H, C(CH_3)$_3$). ^{13}C NMR (126 MHz, DMSO-d_6) δ 161.18 (*C*H═N), 156.11, 150.78, 149.87, 135.68, 135.15, 125.86, 123.53, 119.81, 118.99, 114.44, 94.18, 92.2, 90.36, 86.61, 82.05, 55.38, 34.83 (*C*(CH$_3$)$_3$), 31.73 (C(*C*H$_3$)$_3$), 10.13 (Cp*−*C*H$_3$), 9.43 (Cp*−*C*H$_3$), 9.27 (Cp*−*C*H$_3$), 8.84 (Cp*−*C*H$_3$), 8.01 (Cp*−*C*H$_3$). ESI-MS (*m*/*z*): calcd for $C_{27}H_{34}IrN_2$ 579.23512, found 579.23330, [M−Cl]$^+$. Elemental analysis: calcd for $C_{27}H_{34}IrN_2Cl$: C, 52.80; H, 5.58; N, 4.56, found: C, 53.12; H, 5.31; N, 4.31

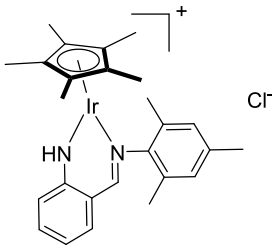

Ir2. (58 mg, Yield 48%). ^{1}H NMR (500 MHz, CDCl$_3$) δ 15.31 (s, 1H, N*H*), 8.84 (s, 1H, C*H*═N), 8.62 (s, 1H), 7.70 (s, 1H), 7.45 (d, *J* = 7.2 Hz, 1H), 7.30 (s, 1H), 7.09 (s, 2H), 2.45 (s, 3H, CH_3), 1.98 (s, 6H, CH_3), 1.72 (s, 15H, Cp*−CH_3). ^{13}C NMR (126 MHz, CDCl$_3$) δ 160.44 (*C*H═N), 143.13, 137.25, 137.11, 136.60, 135.68, 135.19, 130.12, 129.89, 129.31, 128.15, 121.18, 116.38, 93.88, 90.96, 85.40, 20.64 (*C*H$_3$), 17.89 (*C*H$_3$), 9.60 (Cp*−*C*H$_3$), 8.49 (Cp*−*C*H$_3$), 8.44 (Cp*−*C*H$_3$). ESI-MS (*m*/*z*): calcd for $C_{26}H_{32}IrN_2$ 565.21947, found 565.21745 [M−Cl]$^+$. Elemental analysis: calcd for $C_{26}H_{32}IrN_2Cl$: C, 52.03; H, 5.37; N, 4.67, found: C, 52.42; H, 5.16; N, 4.33

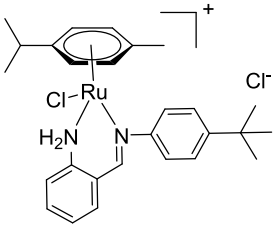

Ru1. (54 mg, Yield 48%). ^{1}H NMR (500 MHz, CDCl$_3$) δ 10.13 (s, 1H, NH_2), 8.62 (d, *J* = 7.8 Hz, 1H), 8.30 (s, 1H, C*H*═N), 7.65 (d, *J* = 8.3 Hz, 2H), 7.57 (t, *J* = 7.5 Hz, 1H), 7.49 (d, *J* = 7.4 Hz, 1H), 7.42−7.36 (m, 2H), 7.34 (d, *J* = 7.4 Hz, 1H), 5.81 (s, 1H), 5.45 (d, 2H), 5.20 (s, 1H), 4.95 (s, 1H, NH_2), 2.57 (m, 1H, arene−C*H*(CH$_3$)$_2$), 1.93 (s, 3H, arene−CH_3), 1.29 (s, 9H,C(CH_3)$_3$), 0.86 (d, *J* = 6.7 Hz, 3H, arene−CH(CH_3)$_2$), 0.80 (d, *J* = 6.6 Hz, 3H, arene−CH(CH_3)$_2$). ^{13}C NMR (126 MHz, DMSO-d_6) δ 162.76 (*C*H═N), 149.52, 149.71, 144.29, 142.08, 134.27, 127.97, 127.70, 125.84, 125.31, 122.69, 120.56, 116.89, 116.28, 106.35, 100.04, 86.34, 85.48, 31.44 (*C*(CH$_3$)$_3$), 31.24 (C(*C*H$_3$)$_3$), 31.20 (C(*C*H$_3$)$_3$), 31.09 (C(*C*H$_3$)$_3$), 29.93 (*C*H(CH$_3$)$_2$), 21.47 (CH(*C*H$_3$)$_2$), 17.84 (arene−*C*H$_3$). ESI-MS (*m*/*z*): calcd for $C_{27}H_{33}RuN_2$ 487.16872, found 487.16773 [M−Cl−HCl]$^+$. Elemental analysis: calcd for $C_{27}H_{34}RuCl_2N_2$: C, 58.06; H, 6.14; N, 5.02, found: C, 58.35; H, 5.97; N, 4.90.

Ru2. (56 mg, Yield 54%). ^{1}H NMR (500 MHz, CDCl$_3$) δ 10.47 (s, 1H, NH_2), 8.71 (d, *J* = 7.9 Hz, 1H), 8.41 (s, 1H, C*H*═N), 7.71 (d, *J* = 8.0 Hz, 2H), 7.65 (t, *J* = 7.6 Hz, 1H), 7.61 (d, *J* = 7.4 Hz, 1H), 7.44 (t, *J* = 7.4 Hz, 1H), 7.26 (d, *J* = 7.9 Hz, 2H), 5.97 (s, 1H), 5.55 (s, 1H), 5.40 (s, 1H), 5.26 (s, 1H), 5.01 (s, 1H, NH_2), 2.63 (m, 1H,

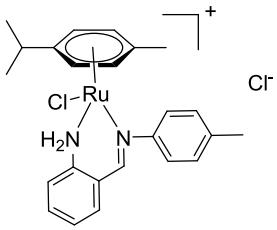

C*H*(CH$_3$)$_2$), 2.42 (s, 3H, Aryl−CH_3), 2.00 (s, 3H, arene−CH_3), 0.91 (d, *J* = 6.9 Hz, 6H, CH(CH_3)$_2$). ^{13}C NMR (126 MHz, DMSO-d_6) δ 162.76 (*C*H═N), 149.51, 147.92, 142.08, 127.97, 127.71, 125.85, 125.35, 125.32, 124.14, 120.57, 116.90, 114.66, 106.35, 100.05, 86.34, 85.48, 63.32, 31.45 (*C*H$_3$), 31.09 (C(*C*H$_3$)$_3$), 29.94 (*C*H(CH$_3$)$_2$), 21.48 (CH(*C*H$_3$)$_2$), 17.85 (arene−*C*H$_3$). ESI-MS (*m*/*z*): calcd for $C_{24}H_{27}RuN_2$ 445.12177, found 445.12113 [M−Cl−HCl]$^+$. Elemental analysis: calcd for $C_{24}H_{28}RuCl_2N_2$: C, 55.81; H, 5.46; N, 5.42, found: C, 56.12; H, 5.33; N, 5.52.

4.1.2. Synthesis of Iridium(III) and Ruthenium(II) Complexes with PF6$^-$ As the Counteranion. The complexes **Ir3**−**Ir8** and **Ru3**−**Ru7** were synthesized by the reaction of bimetallic metal precursors, ligands, and NH_4PF_6 (molar ratio, 1:2:5) in CH_2Cl_2/CH_3OH (v/v, ca. 1:1) for 6 h at 25 °C. The solvent was removed under vacuum and the residue redissolved in CH_2Cl_2, filtered, and concentrated. Subsequently, *n*-hexane was added to the solution to produce a precipitate, which was subsequently filtered and washed with *n*-hexane. The complexes were subjected to vacuum drying. At room temperature, *n*-hexane was slowly diffused into the CH_2Cl_2 solution to obtain single crystals of **Ir3**, **Ir4**, **Ir6**, **Ir8**, and **Ru4**.

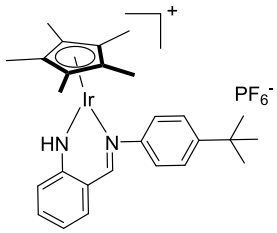

Ir3. (74 mg, Yield 51%). ^{1}H NMR (500 MHz, DMSO-d_6) δ 9.32 (s, 1H, C*H*═N), 7.93 (d, 1H), 7.87 (d, 1H), 7.77 (t, *J* = 7.6 Hz, 1H), 7.62 (d, 2H), 7.31 (m, 3H), 1.60 (s, 15H, Cp*−CH_3), 1.36 (s, 9H, C(CH_3)$_3$). ^{13}C NMR (126 MHz, DMSO-d_6) δ 160.71 (*C*H═N), 155.61, 150.34, 149.32, 135.32, 135.26, 134.79, 134.64, 125.37, 119.38, 118.49, 118.34, 113.96, 93.71, 34.34 (*C*(CH$_3$)$_3$), 31.24 (C(*C*H$_3$)$_3$), 30.93 (C(*C*H$_3$)$_3$), 22.04 (C(*C*H$_3$)$_3$), 13.94 (Cp*−*C*H$_3$), 8.74 (Cp*−*C*H$_3$), 8.20 (Cp*−*C*H$_3$), 8.02 (Cp*−*C*H$_3$). ESI-MS (*m*/*z*): calcd for $C_{27}H_{34}IrN_2$ 579.23512, found 579.23510, [M−PF$_6$]$^+$. Elemental analysis: calcd for $C_{27}H_{34}IrN_2PF_6$: C, 44.81; H, 4.74; N, 3.87, found: C, 45.07; H, 4.61; N, 3.71.

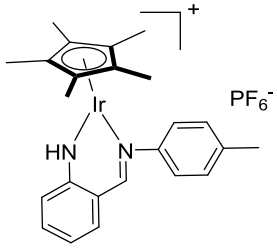

Ir4. (74 mg, Yield 54%).^{1}H NMR (500 MHz, CDCl$_3$) δ 11.97 (s, 1H, N*H*), 8.90 (s, 1H, C*H*═N), 8.00 (d, *J* = 8.7 Hz, 1H), 7.76 (t, *J* = 7.7 Hz, 1H), 7.54 (d, *J* = 8.0 Hz, 1H), 7.38 (d, *J* = 7.6 Hz, 2H), 7.36 (m, 1H), 7.11 (d, *J* = 7.5 Hz, 2H), 2.53 (s, 3H, CH_3), 1.66 (s, 15H, Cp*−CH_3). ^{13}C NMR (126 MHz, DMSO-d_6) δ 160.88 (*C*H═N), 130.16, 129.30, 129.03, 123.34, 117.31, 93.67, 92.09, 63.41, 20.47 (*C*H$_3$), 8.84 (Cp*−*C*H$_3$), 8.22 (Cp*−*C*H$_3$). ESI-MS (*m*/*z*): calcd for $C_{24}H_{28}IrN_2$ 537.18817 found 537.19247, [M−PF$_6$]$^+$. Elemental

https://doi.org/10.1021/acs.inorgchem.3c03471
Inorg. Chem. 2023, 62, 21379−21395

analysis: calcd for $C_{24}H_{28}IrN_2PF_6$: C, 42.29; H, 4.14; N, 4.11, found: C, 42.52; H, 4.01; N, 3.98.

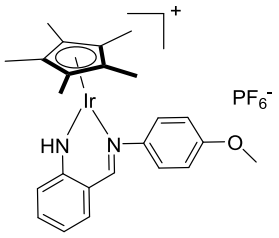

Ir5. (80 mg, Yield 57%). ^{1}H NMR (500 MHz, $CDCl_3$) δ 11.80 (s, 1H, N*H*), 8.82 (s, 1H, C*H*=N), 7.86 (d, J = 6.4 Hz, 1H), 7.66 (m, 3H), 7.33 (d, J = 6.9 Hz, 2H), 7.04 (s, 2H), 3.89 (s, 3H, OCH_3), 1.56 (s, 15H, Cp*−CH_3). ^{13}C NMR (126 MHz, DMSO-d_6) δ 161.24 (*C*H=N), 158.36, 151.75, 149.31, 135.28, 134.74, 124.58, 119.33, 118.42, 113.95, 113.62, 93.70, 55.66, 22.04 (O*C*H$_3$), 13.94 (Cp*−*C*H$_3$), 8.91 (Cp*−*C*H$_3$). ESI-MS (m/z): calcd for $C_{24}H_{28}OIrN_2$ 553.18309, found 553.18330, $[M-PF_6]^+$. Elemental analysis: calcd for $C_{24}H_{28}OIrN_2PF_6$: C, 41.32; H, 4.05; N, 4.02, found: C, 41.76; H, 3.88; N, 3.73.

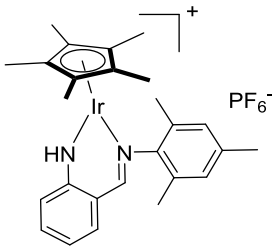

Ir6. (70 mg, Yield 49%). ^{1}H NMR (500 MHz, $CDCl_3$) δ 12.06 (s, 1H, N*H*), 8.68 (s, 1H, C*H*=N), 8.04 (m, 1H), 7.78 (m, 1H), 7.56 (m, 1H), 7.34 (d, J = 3.8 Hz, 1H), 7.13 (s, 2H), 2.46 (s, 3H, CH_3), 2.00 (s, 6H, CH_3), 1.62 (s, 15H, Cp*−CH_3). ^{13}C NMR (126 MHz, $CDCl_3$) δ 161.22 (*C*H=N), 150.39, 137.49, 136.43, 133.74, 129.60, 129.33, 120.41, 120.05, 114.83, 94.07, 20.83 (*C*H$_3$), 17.94 (*C*H$_3$), 8.92 (Cp*−*C*H$_3$). ESI-MS (m/z): calcd for $C_{26}H_{32}IrN_2$ 565.21947, found 565.21838, $[M-PF_6]^+$. Elemental analysis: calcd for $C_{26}H_{32}IrN_2PF_6$: C, 44.00; H, 4.54; N, 3.95, found: C, 44.34; H, 4.32; N, 3.67.

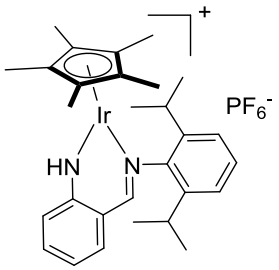

Ir7. (80 mg, Yield 53%). ^{1}H NMR (500 MHz, $CDCl_3$) δ 12.94 (s, 1H, N*H*), 8.77 (s, 1H, C*H*=N), 8.21 (m, 1H), 7.79 (t, J = 7.7 Hz, 1H), 7.46 (d, J = 7.6 Hz, 1H), 7.43−7.37 (m, 3H), 7.33 (d, J = 7.7 Hz, 1H), 3.73 (m, J = 7.0 Hz, 2H, CH(CH_3)$_2$), 1.65 (s, 15H, Cp*−CH_3), 1.38 (d, J = 6.8 Hz, 6H, CH(CH_3)$_2$), 0.96 (d, J = 6.6 Hz, 6H, CH(CH_3)$_2$). ^{13}C NMR (126 MHz, DMSO-d_6) δ 163.92 (*C*H=N), 152.59, 149.76, 140.39, 135.74, 134.74, 128.09, 123.53, 119.60, 118.18, 113.47, 93.87, 27.40 (*C*H(CH$_3$)$_2$), 26.03 (CH(*C*H$_3$)$_2$), 22.55 (CH(*C*H$_3$)$_2$), 8.71 (Cp*−*C*H$_3$). ESI-MS (m/z): calcd for $C_{29}H_{38}IrN_2$ 607.26642, found 607.26467, $[M-PF_6]^+$. Elemental analysis: calcd for $C_{29}H_{38}IrN_2PF_6$: C, 46.33; H, 5.09; N, 3.73, found: C, 46.53; H, 4.87; N, 3.51.

Ir8. (80 mg, Yield 51%). ^{1}H NMR (500 MHz, $CDCl_3$) δ 11.97 (s, 1H, N*H*), 8.96 (s, 1H, C*H*=N), 7.68 (s, 3H), 7.38 (m, 7H), 7.17 (s, 3H), 1.73 (s, 6H, Cp^{ph}−CH_3), 1.49 (s, 6H, Cp^{ph}−CH_3), 1.35 (s, 9H, C(CH_3)$_3$). ^{13}C NMR (126 MHz, DMSO-d_6) δ 161.42 (CH=N), 155.57, 150.43, 149.42, 135.54, 134.88, 134.86, 130.43, 130.33, 128.98, 128.32, 125.31, 123.15, 119.85, 118.48, 114.12, 100.62, 99.71, 91.55, 49.89 (*C*(CH$_3$)$_3$), 34.32 (C(*C*H$_3$)$_3$), 31.20 (C(CH$_3$)$_3$), 9.46 (Cp^{ph}−*C*H$_3$), 8.36 (Cp^{ph}−*C*H$_3$). ESI-MS (m/z): calcd for $C_{32}H_{36}IrN_2$ 641.25077, found 641.25086 $[M-PF_6]^+$. Elemental analysis: calcd for $C_{32}H_{36}IrN_2PF_6$: C, 48.91; H, 4.62; N, 3.56, found: C, 49.02; H, 4.58; N, 3.26.

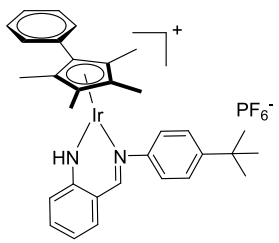

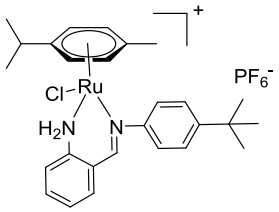

Ru3. (71 mg, Yield 53%). ^{1}H NMR (500 MHz, $CDCl_3$) δ 8.42 (s, 1H, C*H*=N), 7.98 (d, J = 7.6 Hz, 1H), 7.68 (d, J = 7.2 Hz, 3H), 7.57 (s, 1H), 7.49 (d, 3H), 5.59 (s, 1H), 5.46 (s, 1H), 5.38 (d, 2H), 5.23 (s, 1H, NH_2), 2.77 (m, 1H, C*H*(CH$_3$)$_2$), 1.95 (s, 3H, arene−CH_3), 1.39 (s, 9H, C(CH_3)$_3$), 0.97 (s, 6H, CH(CH_3)$_2$). ^{13}C NMR (126 MHz, DMSO-d_6) δ 163.34 (*C*H=N), 135.03, 129.29, 128.49, 125.88, 123.13, 116.86, 115.19, 100.56, 97.04, 86.84, 85.98, 83.07, 63.83, 34.87 (*C*(CH$_3$)$_3$), 31.59 (C(*C*H$_3$)$_3$), 30.45 (C(CH$_3$)$_3$), 24.46 (*C*H(CH$_3$)$_2$), 22.54 (CH(*C*H$_3$)$_2$), 21.96 (CH(*C*H$_3$)$_2$), 14.44 (arene−*C*H$_3$). ESI-MS (m/z): calcd for $C_{27}H_{33}RuN_2$ 487.16872, found 487.16869, $[M-PF_6-HCl]^+$; calcd for $C_{27}H_{34}RuClN_2$ 523.14540, found 523.14390, $[M-PF_6]^+$. Elemental analysis: calcd for $C_{27}H_{34}RuClN_2PF_6$: C, 48.54; H, 5.13; N, 4.19, found: C, 48.78; H, 4.97; N, 4.02.

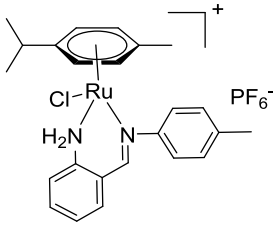

Ru4. (69 mg, Yield 55%). ^{1}H NMR (500 MHz, $CDCl_3$) δ 8.40 (s, 1H, C*H*=N), 7.92 (d, J = 7.2 Hz, 1H), 7.73−7.62 (m, 4H), 7.48 (t, J = 7.4 Hz, 1H), 7.27 (s, 2H), 5.32 (m, 4H), 5.22 (s, 1H, NH_2), 2.56−2.48 (m, 1H, C*H*(CH$_3$)$_2$), 2.41 (s, 3H, Aryl−CH_3), 1.90 (s, 3H, arene−CH_3), 0.91 (d, 6H, CH(CH_3)$_2$). ^{13}C NMR (126 MHz, DMSO-d_6) δ 162.82 (*C*H=N), 153.48, 139.69, 134.35, 129.14, 123.09, 121.46, 96.48, 86.37, 85.51, 85.00, 84.04, 81.66, 80.08, 30.08 (*C*H$_3$), 21.49 (CH(*C*H$_3$)$_2$), 20.59 (CH(*C*H$_3$)$_2$), 17.86 (arene−*C*H$_3$). ESI-MS (m/z): calcd for $C_{24}H_{27}RuN_2$ 445.12177, found 445.12189, $[M-PF_6-HCl]^+$; calcd for $C_{24}H_{28}RuClN_2$ 481.09845, found 481.09703, $[M-PF_6]^+$. Elemental analysis: calcd for $C_{24}H_{28}RuClN_2PF_6$: C, 46.05; H, 4.51; N, 4.48, found: C, 46.37; H, 4.14; N, 4.29.

Ru5. (60 mg, Yield 47%). ^{1}H NMR (500 MHz, $CDCl_3$) δ 8.54 (s, 1H, C*H*=N), 7.93 (s, 1H), 7.70−7.57 (m, 4H), 7.45 (t, J = 7.3 Hz, 1H), 7.05 (s, 2H), 5.53 (m, 4H), 5.44 (s, 1H, NH_2), 3.91 (s, 3H, OCH_3), 2.54−2.42 (m, 1H, C*H*(CH$_3$)$_2$), 1.97 (s, 3H, arene−CH_3), 1.01 (s, 6H, CH(CH_3)$_2$). ^{13}C NMR (126 MHz, DMSO-d_6) δ 162.62 (*C*H=N), 134.68, 129.28, 128.42, 125.10, 115.34, 114.21, 86.84,

https://doi.org/10.1021/acs.inorgchem.3c03471
Inorg. Chem. 2023, 62, 21379−21395

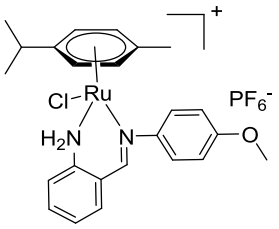

85.98, 55.98, 31.42 (OCH_3), 30.56 ($CH(CH_3)_2$), 24.45 ($CH(CH_3)_2$), 22.53 ($CH(CH_3)_2$), 14.43 (arene−CH_3). ESI-MS (m/z): calcd for $C_{24}H_{27}ORuN_2$ 461.11669, found 461.11581, $[M-PF_6-HCl]^+$; calcd for $C_{24}H_{28}ORuClN_2$ 497.09337, found 497.09254, $[M-PF_6]^+$. Elemental analysis: calcd for $C_{24}H_{28}ORuClN_2PF_6$: C, 44.90; H, 4.40; N, 4.36, found: C, 45.12; H, 4.17; N, 4.15.

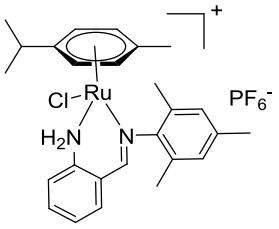

Ru6. (60 mg, Yield 46%). ^{1}H NMR (500 MHz, $CDCl_3$) δ 13.45 (s, 1H, NH_2), 8.52 (s, 1H, CH═N), 8.11 (d, J = 8.6 Hz, 1H), 7.65 (t, J = 7.2 Hz, 1H), 7.51 (m, 2H), 7.17 (s, 2H), 5.64 (d, 2H), 5.51 (d, J = 6.3 Hz, 2H), 2.49 (s, 3H, arene−CH_3), 2.38 (m, 1H, $CH(CH_3)_2$), 2.04 (s, 6H, Aryl−CH_3), 2.02 (s, 3H, Aryl−CH_3), 1.15 (d, J = 6.9 Hz, 6H, $CH(CH_3)_2$). ^{13}C NMR (126 MHz, $CDCl_3$) δ 162.44 (CH═N), 155.49, 151.05, 137.18, 135.44, 133.84, 129.36, 129.28, 121.59, 120.38, 113.98, 105.09, 94.60, 82.50, 31.85 (CH_3), 23.41 ($CH(CH_3)_2$), 20.98 ($CH(CH_3)_2$), 19.62 ($CH(CH_3)_2$), 18.16 (arene−CH_3). ESI-MS (m/z): calcd for $C_{26}H_{31}RuN_2$ 473.15307, found 473.15195, $[M-PF_6-HCl]^+$. Elemental analysis: calcd for $C_{26}H_{32}RuClN_2PF_6$: C, 47.75; H, 4.93; N, 4.28, found: C, 48.06; H, 4.75; N, 4.11.

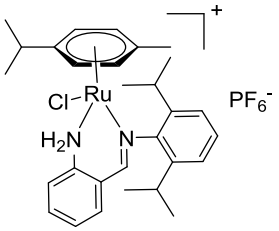

Ru7. (67 mg, Yield 48%). ^{1}H NMR (500 MHz, $CDCl_3$) δ 13.67 (s, 1H, NH_2), 8.55 (s, 1H, CH═N), 8.17 (d, J = 8.7 Hz, 1H), 7.72−7.65 (m, 1H), 7.52−7.49 (m, 1H), 7.46−7.40 (m, 4H), 5.64 (d, J = 6.5 Hz, 2H), 5.60 (d, J = 6.3 Hz, 2H), 3.72 (m, 2H, $CH(CH_3)_2$), 2.65 (m, 1H, arene−$CH(CH_3)_2$), 2.02 (s, 3H, arene−CH_3), 1.43 (d, J = 6.8 Hz, 6H, $CH(CH_3)_2$), 1.15 (d, J = 6.9 Hz, 6H, arene−$CH(CH_3)_2$), 0.95 (d, J = 6.7 Hz, 6H, $CH(CH_3)_2$). ^{13}C NMR (126 MHz, DMSO-d_6) δ 164.29 (CH═N), 154.78, 150.03, 140.21, 135.10, 134.99, 120.70, 123.63, 120.87, 84.69, 81.85, 30.50 ($CH(CH_3)_2$), 27.98 ($CH(CH_3)_2$), 26.14 ($CH(CH_3)_2$), 23.33 ($CH(CH_3)_2$), 22.92 ($CH(CH_3)_2$), 22.54 ($CH(CH_3)_2$), 18.59 (arene−CH_3). ESI-MS (m/z): calcd for $C_{29}H_{37}RuN_2$ 515.20002, found 515.20023, $[M-PF_6-HCl]^+$. Elemental analysis: calcd for $C_{29}H_{38}RuClN_2PF_6$: C, 50.04; H, 5.50; N, 4.02, found: C, 50.24; H, 5.26; N, 3.85.

4.1.3. Synthesis of 16-Electron Ruthenium(II) Complex Ru8. The complex **Ru8** was synthesized by the reaction of **Ru3** with NaOAc (molar ratio: approximately 1:1.5) in CH_2Cl_2/CH_3OH (v/v, ca. 1:1) for 6 h at 25 °C. The solvent was removed under vacuum and the residue redissolved in CH_2Cl_2, filtered, and concentrated. Subsequently, *n*-hexane was added to the solution to produce a precipitate, which was subsequently filtered and washed with *n*-hexane. The complexes were subjected to vacuum drying. At room temperature, *n*-hexane was slowly diffused into a CH_2Cl_2 solution to obtain a single crystal of complex **Ru8**.

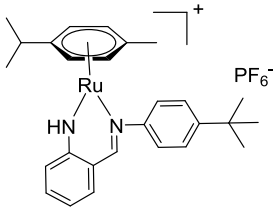

Ru8. (60 mg, Yield 95%). ^{1}H NMR (500 MHz, $CDCl_3$) δ 13.28 (s, 1H, NH), 8.75 (s, 1H, CH═N), 8.04 (d, J = 8.6 Hz, 1H), 7.65 (d, J = 8.3 Hz, 2H), 7.60 (t, J = 7.6 Hz, 1H), 7.49 (d, J = 8.0 Hz, 1H), 7.39 (m, 3H), 5.72 (d, J = 6.2 Hz, 2H), 5.59 (d, J = 6.2 Hz, 2H), 2.04 (s, 3H, arene−CH_3), 1.48 (s, 9H, $C(CH_3)_3$), 1.11 (d, J = 6.9 Hz, 6H, $CH(CH_3)_2$). ^{13}C NMR (126 MHz, DMSO-d_6) δ 163.35 (CH═N), 158.17, 151.99, 135.94, 129.28, 126.55, 125.91, 123.82, 119.90, 114.11, 100.75, 88.11, 84.44, 55.36, 34.88 ($CH(CH_3)_2$), 33.46 ($CH(CH_3)_2$), 31.68 ($CH(CH_3)_2$), 30.56 ($CH(CH_3)_2$), 24.45 ($CH(CH_3)_2$), 22.53 ($CH(CH_3)_2$), 18.63 ($CH(CH_3)_2$), 14.43 (arene−CH_3). ESI-MS (m/z): calcd for $C_{27}H_{33}RuN_2$ 487.16872, found 487.16846, $[M-PF_6]^+$. Elemental analysis: calcd for $C_{27}H_{33}RuN_2PF_6$: C, 51.34; H, 5.27; N, 4.44, found: C, 51.68; H, 5.02; N, 4.17.

■ ASSOCIATED CONTENT

Supporting Information

The Supporting Information is available free of charge at https://pubs.acs.org/doi/10.1021/acs.inorgchem.3c03471.

Additional experimental details and methods, ^{1}H, ^{13}C-{^{1}H} NMR spectra, and ESI-MS spectra for all compounds (Figures S1−S79 and Tables S1−S8) (PDF)

Accession Codes

CCDC 2296029 (**Ir1**), 2296030 (**Ir2**), 2296031 (**Ir3**), 2296033 (**Ir4**), 2296034 (**Ir6**), 2296037 (**Ir8**), 2296039 (**Ru4**) and 2296042 (**Ru8**), contain the supplementary crystallographic data for this paper. These data can be obtained free of charge via www.ccdc.cam.ac.uk/data_request/cif, or by emailing data_request@ccdc.cam.ac.uk, or by contacting The Cambridge Crystallographic Data Centre, 12 Union Road, Cambridge CB2 1EZ, UK; fax: + 441223 336033.

■ AUTHOR INFORMATION

Corresponding Authors

Lihua Guo − *Key Laboratory of Life-Organic Analysis of Shandong Province, Key Laboratory of Green Natural Products and Pharmaceutical Intermediates in Colleges and Universities of Shandong Province, School of Chemistry and Chemical Engineering, Qufu Normal University, Qufu 273165, P. R. China;* orcid.org/0000-0002-0842-9958; Email: guolihua@qfnu.edu.cn

Zhe Liu − *Key Laboratory of Life-Organic Analysis of Shandong Province, Key Laboratory of Green Natural Products and Pharmaceutical Intermediates in Colleges and Universities of Shandong Province, School of Chemistry and Chemical Engineering, Qufu Normal University, Qufu 273165, P. R. China;* orcid.org/0000-0001-5796-4335; Email: liuzheqd@163.com

Authors

Pengwei Li − *Key Laboratory of Life-Organic Analysis of Shandong Province, Key Laboratory of Green Natural Products and Pharmaceutical Intermediates in Colleges and Universities of Shandong Province, School of Chemistry and Chemical Engineering, Qufu Normal University, Qufu 273165, P. R. China*

Jiaxing Li − *Key Laboratory of Life-Organic Analysis of Shandong Province, Key Laboratory of Green Natural Products and Pharmaceutical Intermediates in Colleges and Universities of Shandong Province, School of Chemistry and Chemical Engineering, Qufu Normal University, Qufu 273165, P. R. China*

Yuwen Gong − *Key Laboratory of Life-Organic Analysis of Shandong Province, Key Laboratory of Green Natural Products and Pharmaceutical Intermediates in Colleges and Universities of Shandong Province, School of Chemistry and Chemical Engineering, Qufu Normal University, Qufu 273165, P. R. China*

Xiaoyuan Li − *Key Laboratory of Life-Organic Analysis of Shandong Province, Key Laboratory of Green Natural Products and Pharmaceutical Intermediates in Colleges and Universities of Shandong Province, School of Chemistry and Chemical Engineering, Qufu Normal University, Qufu 273165, P. R. China*

Tingjun Wen − *Key Laboratory of Life-Organic Analysis of Shandong Province, Key Laboratory of Green Natural Products and Pharmaceutical Intermediates in Colleges and Universities of Shandong Province, School of Chemistry and Chemical Engineering, Qufu Normal University, Qufu 273165, P. R. China*

Xinxin Wu − *Key Laboratory of Life-Organic Analysis of Shandong Province, Key Laboratory of Green Natural Products and Pharmaceutical Intermediates in Colleges and Universities of Shandong Province, School of Chemistry and Chemical Engineering, Qufu Normal University, Qufu 273165, P. R. China*

Xinyi Yang − *Key Laboratory of Life-Organic Analysis of Shandong Province, Key Laboratory of Green Natural Products and Pharmaceutical Intermediates in Colleges and Universities of Shandong Province, School of Chemistry and Chemical Engineering, Qufu Normal University, Qufu 273165, P. R. China*

Complete contact information is available at: https://pubs.acs.org/10.1021/acs.inorgchem.3c03471

Notes

The authors declare no competing financial interest.

■ ACKNOWLEDGMENTS

The authors thank the Natural Science Foundation of Shandong Province (ZR2022MB038), the Young Talents Invitation Program of Shandong Provincial Colleges and Universities, and the Taishan Scholars Program for support and Li Yankai from Shiyanjia Lab (www.shiyanjia.com) for the single-crystal XRD data analysis.

■ REFERENCES

(1) Wang, X.; Wang, X.; Jin, S.; Muhammad, N.; Guo, Z. Stimuli-responsive therapeutic metallodrugs. *Chem. Rev.* **2019**, *119*, 1138−1192.

(2) Florea, A.-M.; Büsselberg, D. Cisplatin as an anti-tumor drug: cellular mechanisms of activity, drug resistance and induced side effects. *Cancers* **2011**, *3*, 1351−1371.

(3) Peng, K.; Liang, B.-B.; Liu, W.; Mao, Z.-W. What blocks more anticancer platinum complexes from experiment to clinic: Major problems and potential strategies from drug design perspectives. *Coord. Chem. Rev.* **2021**, *449*, No. 214210.

(4) Ho, G. Y.; Woodward, N.; Coward, J. I. Cisplatin versus carboplatin: comparative review of therapeutic management in solid malignancies. *Crit. Rev. Oncol. Hematol.* **2016**, *102*, 37−46.

(5) Cepeda, V.; Fuertes, A. M.; Castilla, J.; Alonso, C.; Quevedo, C.; Pérez, M. J. Biochemical mechanisms of cisplatin cytotoxicity. *Anti-Cancer Agents Med. Chem.* **2007**, *7*, 3−18.

(6) Giaccone, G.; Herbst, R. S.; Manegold, C.; Scagliotti, G.; Rosell, R.; Miller, V.; Natale, R. B.; Schiller, J. H.; Pawel, Jv.; Pluzanska, A.; Gatzemeier, U.; Grous, J.; Ochs, J. S.; Averbuch, S. D.; Wolf, M. K.; Rennie, P.; Fandi, A.; Johnson, D. H. Gefitinib in combination with gemcitabine and cisplatin in advanced non−small-cell lung cancer: a phase III trial—INTACT 1. *J. Clin. Oncol.* **2004**, *22*, 777−784.

(7) Allison, M.; Caramés-Méndez, P.; Hofmann, B. J.; Pask, C. M.; Phillips, R. M.; Lord, R. M.; McGowan, P. C. Cytotoxicity of ruthenium(II) arene complexes containing functionalized ferrocenyl *β*-diketonate ligands. *Organometallics* **2023**, *42*, 1869−1881.

(8) Dorairaj, D. P.; Haribabu, J.; Dharmasivam, M.; Malekshah, R. E.; Mohamed Subarkhan, M. K.; Echeverria, C.; Karvembu, R. Ru(II)-*p*-cymene complexes of furoylthiourea ligands for anticancer applications against breast cancer cells. *Inorg. Chem.* **2023**, *62*, 11761−11774.

(9) Muhammad, N.; Sadia, N.; Zhu, C.; Luo, C.; Guo, Z.; Wang, X. Biotin-tagged platinum(IV) complexes as targeted cytostatic agents against breast cancer cells. *Chem. Commun.* **2017**, *53*, 9971−9974.

(10) Xiong, X.; Liu, L.-Y.; Mao, Z.-W.; Zou, T. Approaches towards understanding the mechanism-of-action of metallodrugs. *Coord. Chem. Rev.* **2022**, *453*, No. 214311.

(11) Karges, J.; Xiong, K.; Blacque, O.; Chao, H.; Gasser, G. Highly cytotoxic copper(II) terpyridine complexes as anticancer drug candidates. *Inorg. Chim. Acta* **2021**, *516*, No. 120137.

(12) Qi, Y. Y.; Gan, Q.; Liu, Y. X.; Xiong, Y. H.; Mao, Z. W.; Le, X. Y. Two new Cu(II) dipeptide complexes based on 5-methyl-2-(2′-pyridyl)benzimidazole as potential antimicrobial and anticancer drugs: Special exploration of their possible anticancer mechanism. *Eur. J. Med. Chem.* **2018**, *154*, 220−232.

(13) Hartinger, C. G.; Jakupec, M. A.; Zorbas-Seifried, S.; Groessl, M.; Egger, A.; Berger, W.; Zorbas, H.; Dyson, P. J.; Keppler, B. K. KP1019, A new redox-active anticancer agent − preclinical development and results of a clinical phase I study in tumor patients. *Chem. Biodiversity* **2008**, *5*, 2140−2155.

(14) Rademaker-Lakhai, J. M.; van den Bongard, D.; Pluim, D.; Beijnen, J. H.; Schellens, J. H. M. A phase I and pharmacological study with imidazolium-trans-DMSO-imidazole-tetrachlororuthenate, a novel ruthenium anticancer agent. *Clin. Cancer Res.* **2004**, *10*, 3717−3727.

(15) Gupta, G.; Kumari, P.; Ryu, J. Y.; Lee, J.; Mobin, S. M.; Lee, C. Y. Mitochondrial localization of highly fluorescent and photostable BODIPY-based ruthenium(II), rhodium(III), and iridium(III) metal complexes. *Inorg. Chem.* **2019**, *58*, 8587−8595.

(16) Romero-Canelón, I.; Sadler, P. J. Next-generation metal anticancer complexes: multitargeting via redox modulation. *Inorg. Chem.* **2013**, *52*, 12276−12291.

(17) Maji, M.; Acharya, S.; Bhattacharya, I.; Gupta, A.; Mukherjee, A. Effect of an imidazole-containing schiff base of an aromatic sulfonamide on the cytotoxic efficacy of N,N-coordinated half-sandwich ruthenium(II) p-cymene complexes. *Inorg. Chem.* **2021**, *60*, 4744−4754.

(18) Rono, C. K.; Chu, W. K.; Darkwa, J.; Meyer, D.; Makhubela, B. C. E. Triazolyl Ru^{II}, Rh^{III}, Os^{II}, and Ir^{III} Complexes as potential anticancer agents: synthesis, structure elucidation, cytotoxicity, and DNA model interaction studies. *Organometallics* **2019**, *38*, 3197−3211.

(19) Konkankit, C. C.; Marker, S. C.; Knopf, K. M.; Wilson, J. J. Anticancer activity of complexes of the third row transition metals, rhenium, osmium, and iridium. *Dalton Trans.* **2018**, *47*, 9934−9974.
(20) Truong, D.; Sullivan, M. P.; Tong, K. K. H.; Steel, T. R.; Prause, A.; Lovett, J. H.; Andersen, J. W.; Jamieson, S. M. F.; Harris, H. H.; Ott, I.; Weekley, C. M.; Hummitzsch, K.; Sohnel, T.; Hanif, M.; Metzler-Nolte, N.; Goldstone, D. C.; Hartinger, C. G. Potent inhibition of thioredoxin reductase by the rh derivatives of anticancer M(arene/Cp*)(NHC)Cl(2) complexes. *Inorg. Chem.* **2020**, *59*, 3281−3289.
(21) Morris, R. E.; Aird, R. E.; del Socorro Murdoch, P.; Chen, H.; Cummings, J.; Hughes, N. D.; Parsons, S.; Parkin, A.; Boyd, G.; Jodrell, D. I.; Sadler, P. J. Inhibition of cancer cell growth by ruthenium(II) arene complexes. *J. Med. Chem.* **2001**, *44*, 3616−3621.
(22) Aird, R. E.; Cummings, J.; Ritchie, A. A.; Muir, M.; Morris, R. E.; Chen, H.; Sadler, P. J.; Jodrell, D. I. In vitro and in vivo activity and cross resistance profiles of novel ruthenium (II) organometallic arene complexes in human ovarian cancer. *Br. J. Cancer* **2002**, *86*, 1652−1657.
(23) Chen, H.; Parkinson, J. A.; Morris, R. E.; Sadler, P. J. Highly selective binding of organometallic ruthenium ethylenediamine complexes to nucleic acids: novel recognition mechanisms. *J. Am. Chem. Soc.* **2003**, *125*, 173−186.
(24) Liu, Z.; Habtemariam, A.; Pizarro, A. M.; Fletcher, S. A.; Kisova, A.; Vrana, O.; Salassa, L.; Bruijnincx, P. C.; Clarkson, G. J.; Brabec, V.; Sadler, P. J. Organometallic half-sandwich iridium anticancer complexes. *J. Med. Chem.* **2011**, *54*, 3011−3026.
(25) Hearn, J. M.; Romero-Canelon, I.; Munro, A. F.; Fu, Y.; Pizarro, A. M.; Garnett, M. J.; McDermott, U.; Carragher, N. O.; Sadler, P. J. Potent organo-osmium compound shifts metabolism in epithelial ovarian cancer cells. *Proc. Natl. Acad. Sci. U.S.A.* **2015**, *112*, E3800−E3805.
(26) Scheffler, I. E. A century of mitochondrial research: achievements and perspectives. *Mitochondrion* **2001**, *1*, 3−31.
(27) Romero-Canelón, I.; Mos, M.; Sadler, P. J. Enhancement of selectivity of an organometallic anticancer agent by redox modulation. *J. Med. Chem.* **2015**, *58*, 7874−7880.
(28) Li, J.; Guo, L.; Tian, Z.; Tian, M.; Zhang, S.; Xu, K.; Qian, Y.; Liu, Z. Novel half-sandwich iridium(iii) imino-pyridyl complexes showing remarkable in vitro anticancer activity. *Dalton Trans.* **2017**, *46*, 15520−15534.
(29) Tian, M.; Li, J.; Zhang, S.; Guo, L.; He, X.; Kong, D.; Zhang, H.; Liu, Z. Half-sandwich ruthenium(II) complexes containing N∧N-chelated imino-pyridyl ligands that are selectively toxic to cancer cells. *Chem. Commun.* **2017**, *53*, 12810−12813.
(30) Tian, Z.; Li, J.; Zhang, S.; Xu, Z.; Yang, Y.; Kong, D.; Zhang, H.; Ge, X.; Zhang, J.; Liu, Z. Lysosome-targeted chemotherapeutics: half-sandwich ruthenium(II) complexes that are selectively toxic to cancer cells. *Inorg. Chem.* **2018**, *57*, 10498−10502.
(31) Aggarwal, V.; Tuli, H. S.; Varol, A.; Thakral, F.; Yerer, M. B.; Sak, K.; Varol, M.; Jain, A.; Khan, M. A.; Sethi, G. Role of reactive oxygen species in cancer progression: molecular mechanisms and recent advancements. *Biomolecules* **2019**, *9*, 735.
(32) Xu, Z.; Kong, D.; He, X.; Guo, L.; Ge, X.; Liu, X.; Zhang, H.; Li, J.; Yang, Y.; Liu, Z. Mitochondria-targeted half-sandwich ruthenium^{II} diimine complexes: anticancer and antimetastasis via ROS-mediated signalling. *Inorg. Chem. Front.* **2018**, *5*, 2100−2105.
(33) Liu, Z.; Li, J.; Kong, D.; Tian, M.; Zhao, Y.; Xu, Z.; Gao, W.; Zhou, Y. Dual functional half-sandwich Ru(II) complexes: lysosome-targeting probes and anticancer agents. *Eur. J. Inorg. Chem.* **2019**, *2019*, 287−294.
(34) Kong, D.; Guo, L.; Tian, M.; Zhang, S.; Tian, Z.; Yang, H.; Tian, Y.; Liu, Z. Lysosome-targeted potent half-sandwich iridium(III) α-diimine antitumor complexes. *Appl. Organomet. Chem.* **2019**, *33*, No. e4633.
(35) Tait, S. W. G.; Green, D. R. Mitochondria and cell death: outer membrane permeabilization and beyond. *Nat. Rev. Mol. Cell Biol.* **2010**, *11*, 621−632.
(36) Sabharwal, S. S.; Schumacker, P. T. Mitochondrial ROS in cancer: initiators, amplifiers or an Achilles' heel? *Nat. Rev. Cancer* **2014**, *14*, 709−721.
(37) Wen, S.; Zhu, D.; Huang, P. Targeting cancer cell mitochondria as a therapeutic approach. *Future Med. Chem.* **2013**, *5*, 53−67.
(38) Nadova, Z.; Lenkavska, L.; Fragola, A.; Bonneau, S.; Sureau, F.; Miskovsky, P. Correlation between mitochondrial morphology and functionality after oxidative stress. *Biophys. J.* **2016**, *110*, 470a.
(39) Murphy, M. P. Slip and leak in mitochondrial oxidative phosphorylation. *Biochim. Biophys. Acta, Bioenerg.* **1989**, *977*, 123−141.
(40) Trapp, S.; Horobin, R. W. A predictive model for the selective accumulation of chemicals in tumor cells. *Eur. Biophys. J.* **2005**, *34*, 959−966.
(41) González Rubio, S.; Montero Pastor, N.; García, C.; Almendro-Vedia, V. G.; Ferrer, I.; Natale, P.; Paz-Ares, L.; Lillo, M. P.; López-Montero, Iván. Enhanced cytotoxic activity of mitochondrial mechanical effectors in human lung carcinoma H520 cells: pharmaceutical implications for cancer therapy. *Front. Oncol.* **2018**, *8*, 514.
(42) Qiu, K.; Chen, Y.; Rees, T. W.; Ji, L.; Chao, H. Organelle-targeting metal complexes: From molecular design to bio-applications. *Coord. Chem. Rev.* **2019**, *378*, 66−86.
(43) Hu, X.; Guo, L.; Liu, M.; Sun, M.; Zhang, Q.; Peng, H.; Zhang, F.; Liu, Z. Formation of iridium(III) and rhodium(III) amine, imine, and amido complexes based on pyridine-amine ligands: structural diversity arising from reaction conditions, substituent variation, and metal centers. *Inorg. Chem.* **2022**, *61*, 10051−10065.
(44) Gao, J.; Guo, L.; Wu, Y.; Cheng, Y.; Hu, X.; Liu, J.; Liu, Z. 16-electron half-sandwich rhodium(III), iridium(III), and ruthenium(II) complexes as lysosome-targeted anticancer agents. *Organometallics* **2021**, *40*, 3999−4010.
(45) Brüggemann, P.; Mzyk, K.; Molter, M.; Nellesen, J.; Schaper, K.; Ganter, C. Synthesis, reactivity and electronic properties of Quinazolin-2-one-Based N-Heterocyclic carbenes. *Eur. J. Inorg. Chem.* **2021**, No. e202100894.
(46) Rigo, B.; Gautret, P.; Akue-Gedu, R.; Lelieur, J.-P. An improved synthesis of methyl 1,3-dihydro-2H-pyrrolo[3,4-b]quinoline-2-carboxylate. *Synthesis* **2007**, *2007*, 3319−3322.
(47) Björgvinsson, M.; Halldorsson, S.; Arnason, I.; Magull, J.; Fenske, D. Preparation and characterization of $(C_5Me_4Ph)TiCl_3$, the oxochloride complexes $[(C_5Me_4Ph)TiCl_2]_2(\mu\text{-}O)$ and $[(C_5Me_4Ph)\text{-}TiCl(\mu\text{-}O)]_3$ and the oxo-complex$[(C_5Me_4Ph)Ti]_4(\mu\text{-}O)_6$. The X-ray crystal structures of $[(C_5Me_4Ph)TiCl_2]_2(\mu\text{-}O)$ and $[(C_5Me_4Ph)\text{-}Ti]_4(\mu\text{-}O)_6$. *J. Org. Chem.* **1997**, *544*, 207−215.
(48) Selvam, P.; De, S.; Paira, P.; Kumar, S. K. A.; Kumar, R. S.; Moorthy, A.; Ghosh, A.; Kuo, Y. C.; Banerjee, S.; Jenifer, S. K. In vitro studies on the selective cytotoxic effect of luminescent Ru(II)-p-cymene complexes of imidazo-pyridine and imidazo quinoline ligands. *Dalton Trans.* **2022**, *51*, 17263−17276.
(49) Panchangam, R. L.; Rao, R. N.; Balamurali, M. M.; Hingamire, T. B.; Shanmugam, D.; Manickam, V.; Chanda, K. Antitumor effects of Ir(III)-2*H*-indazole complexes for triple negative breast cancer. *Inorg. Chem.* **2021**, *60*, 17593−17607.
(50) Uršič, M.; Lipec, T.; Meden, A.; Turel, I. Synthesis and structural evaluation of organo-ruthenium complexes with beta-diketonates. *Molecules* **2017**, *22*, 326.
(51) Dömötör, O.; Pape, V. F. S.; May, N. V.; Szakács, G.; Enyedy, É. A. Comparative solution equilibrium studies of antitumor ruthenium(η^6-p-cymene) and rhodium(η^5-C_5Me_5) complexes of 8-hydroxyquinolines. *Dalton Trans.* **2017**, *46*, 4382−4396.
(52) Arunachalam, A.; Rengan, R.; Umapathy, D.; Arockiam, A. J. V. Impact of biphenyl benzhydrazone-incorporated arene Ru(II) complexes on cytotoxicity and the cancer cell death mechanism. *Organometallics* **2022**, *41*, 2474−2486.
(53) Sathiya Kamatchi, T.; Mohamed Subarkhan, M. K.; Ramesh, R.; Wang, H.; Małecki, J. G. Investigation into antiproliferative activity and apoptosis mechanism of new arene Ru(II) carbazole-based hydrazone complexes. *Dalton Trans.* **2020**, *49*, 11385−11395.

https://doi.org/10.1021/acs.inorgchem.3c03471
Inorg. Chem. 2023, 62, 21379−21395

(54) Guo, L.; Li, P.; Li, J.; Gong, Y.; Li, X.; Liu, Y.; Yu, K.; Liu, Z. Half-sandwich iridium(III), rhodium(III), and ruthenium(II) complexes chelating hybrid sp^2-N/sp^3-N donor ligands to achieve improved anticancer selectivity. *Inorg. Chem.* **2023**, *62*, 15118−15137.
(55) Hohmann, H.; Hellquist, B.; Van Eldik, R. Kinetics and mechanism of the complex formation reactions of diaqua(ethylenediamine)- and diaqua(tetraethylethylenediamine) palladium(II) with the purine nucleosides adenosine and inosine. *Inorg. Chem.* **1992**, *31*, 345−351.
(56) Guo, L.; Zhang, H.; Tian, M.; Tian, Z.; Xu, Y.; Yang, Y.; Peng, H.; Liu, P.; Liu, Z. Electronic effects on reactivity and anticancer activity by half-sandwich N,N-chelated iridium(iii) complexes. *New J. Chem.* **2018**, *42*, 16183−16192.
(57) Zamorano, A.; Rendón, N.; López-Serrano, J.; Álvarez, E.; Carmona, E. Activation of small molecules by the metal−amido bond of rhodium(III) and iridium(III) (η^5-C_5Me_5)M-aminopyridinate complexes. *Inorg. Chem.* **2018**, *57*, 150−162.
(58) Nagashima, H.; Kondo, H.; Hayashida, T.; Yamaguchi, Y.; Gondo, M.; Masuda, S.; Miyazaki, K.; Matsubara, K.; Kirchner, K. Chemistry of coordinatively unsaturated organoruthenium amidinates as entry to homogeneous catalysis. *Coord. Chem. Rev.* **2003**, *245*, 177−190.
(59) Kang, J.; Liu, Y.; Xie, M. X.; Li, S.; Jiang, M.; Wang, Y. D. Interactions of human serum albumin with chlorogenic acid and ferulic acid. *Biochim. Biophys. Acta, Gen. Subj.* **2004**, *1674*, 205−214.
(60) Abou-Zied, O. K.; Al-Shihi, O. I. K. Characterization of subdomain IIA binding site of human serum albumin in its native, unfolded, and refolded states using small molecular probes. *J. Am. Chem. Soc.* **2008**, *130*, 10793−10801.
(61) Ding, F.; Zhao, G.; Huang, J.; Sun, Y.; Zhang, L. Fluorescence spectroscopic investigation of the interaction between chloramphenicol and lysozyme. *Eur. J. Med. Chem.* **2009**, *44*, 4083−4089.
(62) Johansson, J. S.; Eckenhoff, R. G.; Dutton, P. L. Binding of halothane to serum albumin demonstrated using tryptophan fluorescence. *Anesthesiology* **1995**, *83*, 316−324.
(63) Yang, Y.; Guo, L.; Tian, Z.; Gong, Y.; Zheng, H.; Zhang, S.; Xu, Z.; Ge, X.; Liu, Z. Novel and versatile imine-N-heterocyclic carbene half-sandwich Iridium(III) complexes as lysosome-targeted anticancer agents. *Inorg. Chem.* **2018**, *57*, 11087−11098.
(64) Ruiz, J.; Vicente, C.; de Haro, C.; Bautista, Delia. Novel bis-C,N-cyclometalated Iridium(III) thiosemicarbazide antitumor complexes: interactions with human serum albumin and DNA, and inhibition of cathepsin B. *Inorg. Chem.* **2013**, *52*, 974−982.
(65) He, W.; Li, Y.; Xue, C.; Hu, Z.; Chen, X.; Sheng, F. Effect of Chinese medicine alpinetin on the structure of human serum albumin. *Bioorg. Med. Chem.* **2005**, *13*, 1837−1845.
(66) Samari, F.; Hemmateenejad, B.; Shamsipur, M.; Rashidi, M.; Samouei, H. Affinity of Two Novel Five-Coordinated Anticancer Pt(II) Complexes to Human and Bovine Serum Albumins: A Spectroscopic Approach. *Inorg. Chem.* **2012**, *51*, 3454−3464.
(67) Castiñeiras, A.; Fernández-Hermida, N.; García-Santos, I.; Gómez-Rodríguez, L. Neutral Ni^{II}, Pd^{II} and Pt^{II} ONS-pincer complexes of 5-acetylbarbituric-4N-dimethylthiosemicarbazone: synthesis, characterization and properties. *Dalton Trans.* **2012**, *41*, 13486−13495.
(68) Schutte, B.; Nieland, L.; van Engeland, M.; Henfling, M. E. R.; Meijer, L.; Ramaekers, F. C. S. The Effect of the Cyclin-Dependent Kinase Inhibitor Olomoucine on Cell Cycle Kinetics. *Exp. Cell Res.* **1997**, *236*, 4−15.
(69) Dan Dunn, J.; Alvarez, L. A.; Zhang, X.; Soldati, T. Reactive oxygen species and mitochondria: A nexus of cellular homeostasis. *Redox Biol.* **2015**, *6*, 472−485.
(70) Trachootham, D.; Alexandre, J.; Huang, P. Targeting cancer cells by ROS-mediated mechanisms: a radical therapeutic approach? *Nat. Rev. Drug Discovery* **2009**, *8*, 579−591.
(71) Zorov, D. B.; Juhaszova, M.; Sollott, S. J. Mitochondrial reactive oxygen species (ROS) and ROS-induced ROS release. *Physiol. Rev.* **2014**, *94*, 909−950.
(72) Jeong, C.-H.; Joo, S. H. Downregulation of reactive oxygen species in apoptosis. *J. Cancer Prev.* **2016**, *21*, 13−20.
(73) Circu, M. L.; Aw, T. Y. Reactive oxygen species, cellular redox systems, and apoptosis. *Free Radical Biol. Med.* **2010**, *48*, 749−762.
(74) Perry, G.; Raina, A. K.; Nunomura, A.; Wataya, T.; Sayre, L. M.; Smith, M. A. How important is oxidative damage? Lessons from Alzheimer's disease. *Free Radical Biol. Med.* **2000**, *28*, 831−834.
(75) Liu, Z.; Romero-Canelón, I.; Habtemariam, A.; Clarkson, G. J.; Sadler, P. J. Potent half-Sandwich Iridium(III) anticancer complexes containing C^N-chelated and pyridine ligands. *Organometallics* **2014**, *33*, 5324−5333.
(76) Liu, Z.; Sadler, P. J. Organoiridium complexes: anticancer agents and catalysts. *Acc. Chem. Res.* **2014**, *47*, 1174−1185.
(77) Liu, Z.; Romero-Canelón, I.; Qamar, B.; Hearn, J. M.; Habtemariam, A.; Barry, N. P.; Pizarro, A. M.; Clarkson, G. J.; Sadler, P. J. The potent oxidant anticancer activity of organoiridium catalysts. *Angew. Chem., Int. Ed.* **2014**, *53*, 3941−3946.
(78) Acharya, A.; Das, I.; Chandhok, D.; Saha, T. Redox regulation in cancer: a double-edged sword with therapeutic potential. *Oxid. Med. Cell. Longevity* **2010**, *3*, No. 702528.
(79) Ye, Y.; Zhang, T.; Yuan, H.; Li, D.; Lou, H.; Fan, P. Mitochondria-targeted lupane triterpenoid derivatives and their selective apoptosis-inducing anticancer mechanisms. *J. Med. Chem.* **2017**, *60*, 6353−6363.
(80) Kozieł, S.; Komarnicka, U. K.; Ziółkowska, A.; Skórska-Stania, A.; Pucelik, B.; Płotek, M.; Sebastian, V.; Bieńko, A.; Stochel, G.; Kyzioł, A. Anticancer potency of novel organometallic Ir(III) complexes with phosphine derivatives of fluoroquinolones encapsulated in polymeric micelles. *Inorg. Chem. Front.* **2020**, *7*, 3386−3401.
(81) Azzopardi, M.; Farrugia, G.; Balzan, R. Cell-cycle involvement in autophagy and apoptosis in yeast. *Mech. Ageing Dev.* **2017**, *161*, 211−224.
(82) Friedl, P.; Alexander, S. Cancer invasion and the microenvironment: plasticity and reciprocity. *Cell* **2011**, *147*, 992−1009.
(83) Valastyan, S.; Weinberg, R. A. Tumor metastasis: molecular insights and evolving paradigms. *Cell* **2011**, *147*, 275−292.
(84) Newby, A. C. Matrix metalloproteinases regulate migration, proliferation, and death of vascular smooth muscle cells by degrading matrix and non-matrix substrates. *Cardiovasc. Res.* **2006**, *69*, 614−624.
(85) Gialeli, C.; Theocharis, A. D.; Karamanos, N. K. Roles of matrix metalloproteinases in cancer progression and their pharmacological targeting. *FEBS J.* **2011**, *278*, 16−27.

https://doi.org/10.1021/acs.inorgchem.3c03471
Inorg. Chem. 2023, 62, 21379−21395